

UNCLASSIFIED

AD NUMBER

ADB017853

LIMITATION CHANGES

TO:

Approved for public release; distribution is unlimited.

FROM:

Distribution authorized to U.S. Gov't. agencies only; Test and Evaluation; APR 1977. Other requests shall be referred to Air Force Armament Laboratory, Attn: DLMA, Eglin AFB, FL 32542.

AUTHORITY

AEDC ltr, 4 Sep 1980

THIS PAGE IS UNCLASSIFIED

AEDC-TR-77-31
AFATL-TR-77-23

MAY 1977
JUN 1977

Cy. 2



FORCE AND MOMENT CHARACTERISTICS OF A MATRIX OF OGIVE-CYLINDER CONFIGURATIONS AT MACH NUMBERS FROM 1.5 TO 4.0

**VON KÁRMÁN GAS DYNAMICS FACILITY
ARNOLD ENGINEERING DEVELOPMENT CENTER
AIR FORCE SYSTEMS COMMAND
ARNOLD AIR FORCE STATION, TENNESSEE 37389**

April 1977

Final Report for Period February 10 - July 20, 1976

Distribution limited to U.S. Government agencies only; this report contains information on test and evaluation of military hardware; April 1977; other requests for this document must be referred to Air Force Armament Laboratory (DLMA), Eglin AFB, Florida 32542.

Prepared for

**AIR FORCE ARMAMENT LABORATORY (DLMA)
EGLIN AIR FORCE BASE, FLORIDA 32542**

Property of U.S. Air Force

**US ARMY MISSILE COMMAND (AMSMI-RDK)
REDSTONE ARSENAL, ALABAMA 35089**

**AIR FORCE FLIGHT DYNAMICS LABORATORY (FGCB)
WRIGHT-PATTERSON AIR FORCE BASE, OHIO 45433**

NOTICES

When U. S. Government drawings specifications, or other data are used for any purpose other than a definitely related Government procurement operation, the Government thereby incurs no responsibility nor any obligation whatsoever, and the fact that the Government may have formulated, furnished, or in any way supplied the said drawings, specifications, or other data, is not to be regarded by implication or otherwise, or in any manner licensing the holder or any other person or corporation, or conveying any rights or permission to manufacture, use, or sell any patented invention that may in any way be related thereto.

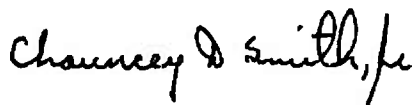
Qualified users may obtain copies of this report from the Defense Documentation Center.

References to named commercial products in this report are not to be considered in any sense as an endorsement of the product by the United States Air Force or the Government.

APPROVAL STATEMENT

This technical report has been reviewed and is approved for publication.

FOR THE COMMANDER



CHAUNCEY D. SMITH, JR.
Lt Colonel, USAF
Chief Air Force Test Director, VKF
Directorate of Test



ALAN L. DEVEREAUX
Colonel, USAF
Director of Test

UNCLASSIFIED

REPORT DOCUMENTATION PAGE		READ INSTRUCTIONS BEFORE COMPLETING FORM
1. REPORT NUMBER AEDC-TR-77-31 AFATL-TR-77-23	2. GOVT ACCESSION NO.	3. RECIPIENT'S CATALOG NUMBER
4. TITLE (and Subtitle) FORCE AND MOMENT CHARACTERISTICS OF A MATRIX OF OGIVE-CYLINDER CONFIGURATIONS AT MACH NUMBERS FROM 1.5 TO 4.0		5. TYPE OF REPORT & PERIOD COVERED Final Report - February 10 - July 20, 1976
		6. PERFORMING ORG. REPORT NUMBER
7. AUTHOR(s) J. L. Jordan, ARO, Inc.		8. CONTRACT OR GRANT NUMBER(s)
9. PERFORMING ORGANIZATION NAME AND ADDRESS Arnold Engineering Development Center (XO) Air Force Systems Command Arnold Air Force Station, Tennessee 37389		10. PROGRAM ELEMENT, PROJECT, TASK AREA & WORK UNIT NUMBERS Program Element 63601F System 670E Task 01
11. CONTROLLING OFFICE NAME AND ADDRESS Air Force Armament Laboratory (DLMA) Eglin AFB, Florida 32542		12. REPORT DATE April 1977
		13. NUMBER OF PAGES 64
14. MONITORING AGENCY NAME & ADDRESS (if different from Controlling Office)		15. SECURITY CLASS. (of this report) UNCLASSIFIED
		15a. DECLASSIFICATION/DOWNGRADING SCHEDULE N/A
16. DISTRIBUTION STATEMENT (of this Report) Distribution limited to U.S. Government agencies only; this report contains information on test and evaluation of military hardware; April 1977; other requests for this document must be referred to Air Force Armament Laboratory (DLMA), Eglin AFB, Florida 32542.		
17. DISTRIBUTION STATEMENT (of the abstract entered in Block 20, if different from Report)		
18. SUPPLEMENTARY NOTES Available in DDC		
19. KEY WORDS (Continue on reverse side if necessary and identify by block number) force (axial) projectiles moment Mach numbers characteristics Reynolds number ogives static stability		
20. ABSTRACT (Continue on reverse side if necessary and identify by block number) Tests were conducted in the Arnold Engineering Development Center (AEDC), von Karman Gas Dynamics Facility (VKF) to determine the static stability and axial-force characteristics of several families of ogive-cylinder configurations over a Mach number range from 1.5 to 4.5. Model combinations of twenty noses and four afterbodies were tested at Mach numbers 1.5, 2.0, 2.5, 3.0, 3.5, 4.0, and 4.5 at a primary test Reynolds number, based on model		

UNCLASSIFIED

UNCLASSIFIED

20. ABSTRACT (Continued)

diameter, of 0.18 million. Configuration variables were nose bluntness and caliber and afterbody caliber. The angle-of-attack range was from -6 to 14 deg. A description of the test program and selected results are presented.

UNCLASSIFIED

PREFACE

The work reported herein was conducted at the Arnold Engineering Development Center (AEDC), Air Force Systems Command (AFSC), at the request of the Air Force Armament Laboratory (AFATL/DLMA), Eglin Air Force Base, Florida (Mr. Carroll B. Butler was the AFATL project monitor); the U.S. Army Missile Command (AMSMI-RDK), Redstone Arsenal, Alabama; and the Air Force Flight Dynamics Laboratory (AFFDL/FGCB), Wright-Patterson Air Force Base, Ohio. The work was conducted under Program Element 63601F, System 670E, Task 01. The results were obtained by ARO, Inc., AEDC Division (a Sverdrup Corporation Company), operating contractor for the AEDC, AFSC, Arnold Air Force Station, Tennessee, under ARO Project No. V42A-H1A. The author of this report was J. L. Jordan, ARO, Inc. The data analysis was completed on August 19, 1976, and the manuscript (ARO Control No. ARO-VKF-TR-77-6) was submitted for publication on February 2, 1977.

CONTENTS

	<u>Page</u>
1.0 INTRODUCTION	5
2.0 APPARATUS	
2.1 Wind Tunnel	5
2.2 Models	6
2.3 Instrumentation and Precision	6
3.0 PROCEDURE	
3.1 Test Conditions	7
3.2 Test Procedure	8
3.3 Data Uncertainty	8
4.0 RESULTS AND DISCUSSION	10
5.0 SUMMARY OF RESULTS	13
REFERENCES	14

ILLUSTRATIONS

Figure

1. Wind Tunnel and Model Injection System	15
2. Model Installation in Tunnel A	16
3. Photographs of Model and Components	17
4. Model Details	22
5. Base Pressure Probe Orientation	27
6. Comparison of Experimental and Theoretical C_{A_0} for Variations in Midbody caliber at $M_\infty = 1.50$	28
7. Effect of Nose Bluntness on Force and Moment Characteristics of the 3.0-caliber Nose Configurations	29
8. Comparison of Experimental and Theoretical C_{A_0} for Variations in Nose Bluntness for the 3.0-caliber Nose Configurations, $M_\infty = 3.01$	33
9. Effect of Nose Bluntness on Force and Moment Characteristics of the 2.25-caliber Nose Configurations, $M_\infty = 3.01$	34
10. Power-Series Nose Shape Force and Moment Characteristics, $M_\infty = 3.01$	36
11. Effect of Nose caliber on Force and Moment Characteristics, $M_\infty = 3.01$	38

<u>Figure</u>	<u>Page</u>
12. Effect of Afterbody Length on Force and Moment Characteristics of the 3.0-caliber Nose Configurations, $M_\infty = 3.01$	42
13. Effect of Mach number on Force and Moment Characteristics of the 3.0-caliber Nose Configurations	46
14. Variation of C_{N_α} , C_{m_α} , and C_{A_0} with Mach Number and Comparisons with Theoretical C_{A_0} for 3.0-caliber Nose Configurations	54
15. Effect of Mach Number on Force and Moment Characteristics of the Power-Series Nose Configurations	55
16. Variation of C_{N_α} , C_{m_α} , and C_{A_0} with Mach Number for the Power-Series Nose Configurations	59
17. Variation of C_{N_α} , C_{m_α} , and C_{A_0} with Mach Number and Comparisons with Subsonic and Transonic Results from Other Test Programs	60

TABLE

1. Test Summary	61
NOMENCLATURE	63

1.0 INTRODUCTION

A broad data base covering a wide variety of configuration variables is necessary to aid in the continuing development of missile and bomb weapon systems. This test program was devised to provide preliminary weapon system design force and moment data on a comprehensive matrix of nose-afterbody geometries at supersonic speeds. Several nose geometries included in the matrix were intended to address immediate requirements of the test sponsors concerning radome designs in support of current development programs. Of prime interest on these configurations was incremental drag caused by nose shape variation at a given attitude. In general, the test objective was to produce a bank of experimental static force and moment data for guided and unguided missile and bomb weapon systems.

The test was conducted during two separate periods in the Arnold Engineering Development Center (AEDC) von Kármán Gas Dynamics Facility (VKF) Supersonic Wind Tunnel (A) at Mach numbers 1.50, 2.00, 2.50, 3.01, 3.47, 4.02, and 4.50 at a primary test Reynolds number of 0.18 million based on model base diameter. This test Reynolds number condition was chosen in an attempt to maintain a laminar boundary layer at each Mach number for the range of model lengths at zero angle of attack. The laminar condition was selected so that pressure drag coefficients for these bodies at $\alpha = 0$ could be obtained from the test data by accounting for the measured base drag and calculated laminar skin-friction drag coefficients. Testing at higher Reynolds numbers, which would have resulted in a mixed laminar-transitional-turbulent condition in most cases, would have made the determination of the appropriate skin-friction drag contribution more uncertain.

Static stability and axial-force data were obtained on various combinations of twenty nose configurations with four afterbody configurations. Each ogive-cylinder configuration formed an axisymmetric body. The effects of nose bluntness, nose caliber, and afterbody caliber were investigated. The angle-of-attack range was from -6 to 14 deg. All data generated during this test will be included in a report published by AFATL.

2.0 APPARATUS

2.1 WIND TUNNEL

Tunnel A (Fig. 1) is a continuous, closed-circuit, variable density wind tunnel with an automatically driven flexible-plate-type nozzle and a 40- by 40-in. test section. The tunnel can be operated at Mach numbers from 1.5 to 6.0 at maximum stagnation pressures from 29 to 200 psia, respectively, and stagnation temperatures up to 750°R ($M_\infty = 6.0$). Minimum operating pressures range from about one-tenth to one-twentieth of the

maximum at each Mach number. The tunnel is equipped with a model injection system which allows removal of the model from the test section while the tunnel remains in operation. A description of the tunnel and airflow calibration information may be found in the Test Facilities Handbook (Ref. 1).

2.2 MODELS

Photographs and details of the models and components are shown in Figs. 2 through 4. All model components were stainless steel and were provided by AFATL. Model components consisted of twenty nose sections and four cylindrical midbodies, each using the same cylindrical afterbody.

The nose geometries included 17 tangent ogive sharp and spherically blunted noses, with bluntness ratios from 0.25 to 0.75, and one hemispherical nose. In addition, there were two power-series noses whose shapes were defined by an exponential function of the nose axial location. The nose lengths ranged from 1 to 4 calibers. The four midbody lengths were 5, 7, 9, and 11 calibers. The single afterbody was 1 caliber long. Total model length ranged from 8.4 to 19.2 in. with a diameter of 1.2 in.

2.3 INSTRUMENTATION AND PRECISION

Tunnel A stilling chamber pressure is measured with a 15-, 60-, 150- or a 300-psid transducer referenced to a near vacuum. Based on periodic comparisons with secondary standards, the uncertainty (a bandwidth which includes 95 percent of the residuals) of these transducers is estimated to be within ± 0.2 percent of reading or ± 0.015 psia, whichever is greater. Stilling chamber temperature is measured with a copper-constantan thermocouple with an uncertainty of $\pm 3^\circ\text{F}$ based on repeat calibrations.

Model forces and moments were measured with six-component, moment type, strain-gage balances supplied by AEDC-Propulsion Wind Tunnel Facility (PWT) and calibrated by VKF. A different balance was used during the second test entry because the first balance was being used in another test at the time. Before each test entry, static loads in each plane and combined static loads were applied to the balance to simulate the range of loads and center-of-pressure locations anticipated during the test. The following uncertainties represent the bands of 95 percent of the measured residuals, based on differences between the applied loads and the corresponding values calculated from the balance calibration equations included in the final data reduction. The range of check loads applied and the measurement uncertainties for each balance are listed on the following page.

Component	Entry 1/Entry 2			
	Balance Design Loads	Calibration Load Range	Range Of Check Loads	Measurement Uncertainty
Normal force, lb	$\pm 20/\pm 10$	$\pm 20/\pm 10$	$\pm 10/\pm 6$	$\pm 0.05/\pm 0.04$
Pitching moment, *in.-lb	$\pm 40/\pm 20$	$\pm 40/\pm 20$	$\pm 6/\pm 4$	$\pm 0.04/\pm 0.03$
Side force, lb	$\pm 20/\pm 10$	$\pm 20/\pm 10$	$\pm 10/\pm 6$	$\pm 0.03/\pm 0.04$
Yawing moment, *in.-lb	$\pm 40/\pm 20$	$\pm 40/\pm 20$	$\pm 6/\pm 4$	$\pm 0.04/\pm 0.02$
Rolling moment, in.-lb	$\pm 6/\pm 2.25$	$\pm 6/\pm 0.9$	$\pm 0.5/\pm 0.5$	$\pm 0.01/\pm 0.03$
Axial force, lb	$\pm 6/\pm 6$	$\pm 6/\pm 6$	0 to 6 0 to 6	$\pm 0.02/\pm 0.02$

*About balance forward moment bridge.

The transfer distances from the balance forward moment bridge to the model moment reference location along the longitudinal axis (see Fig. 4a) were 2.382, 3.588, 4.813, and 5.992 in. for the 5-, 7-, 9-, and 11-caliber midbody sections, respectively, and were measured with an estimated precision of ± 0.005 in.

Base pressures during the pitch-pause data mode were measured with 15-psid transducers referenced to a near vacuum. A 5-psid, fast response pressure transducer was used in conjunction with the 15-psid transducer to obtain base pressure during the continuous sweep data mode. Based on periodic comparisons with secondary standards, the estimated precision of these transducers is 0.003 psi or 0.2 percent of the reading, whichever is greater. Base pressure probe locations are illustrated in Fig. 5.

Model flow-field shadowgraphs or color schlierens were taken on all configurations at selected model attitudes.

3.0 PROCEDURE

3.1 TEST CONDITIONS

The test was conducted at Mach numbers 1.5, 2.0, 2.5, 3.0, 3.5, 4.0, and 4.5. The test Reynolds number, based on model cylinder diameter, was 0.18 million. A summary of the test conditions at each Mach number is given below.

M_∞	P_O , psia	T_O , °R	q_∞ , psia	p_∞ , psia	$Re_d \times 10^{-6}$
1.50	6.5	575	2.80	1.77	0.18
2.00	7.5	575	2.69	0.96	0.18

M_∞	P_o , psia	T_o , °R	q_∞ , psia	p_∞ , psia	$Re_d \times 10^{-6}$
2.50	9.5	575	2.42	0.55	0.18
3.01	13.1	575	2.23	0.35	↓
3.47	16.6	575	1.92	0.23	
4.02	22.0	580	1.60	0.14	
4.50	28.0	580	1.37	0.09	

A test summary, showing all configurations tested and the variables for each, is presented in Table 1.

3.2 TEST PROCEDURE

Data were obtained for an angle-of-attack range of -6 to 14 deg at zero roll angle. Data were also obtained at other roll angles to check for possible model-balance misalignment and flow nonuniformity effects.

To enhance the data acquisition rate, the force and base pressure data were primarily obtained with the continuous sweep technique at a sweep rate of approximately 0.5 deg/sec. Data sampling rate was 1,250 channels/sec, and 15 data loops were averaged for each data point, spanning an angle range of about 0.1 deg. For comparison purposes, conventional pitch-pause-type data were taken periodically throughout the test. For this data acquisition mode, the model was pitched to the desired attitude and data recorded after a preset pause to allow the four base pressures to stabilize.

Insufficient time is available for base pressure stabilization in the sweep mode of testing when the large volume standard pressure system is used. In the sweep mode, therefore, a fast response pressure transducer was employed. The four standard pressures were allowed to stabilize at $\alpha = 0$ before each sweep to obtain a reference base pressure level. The low volume transducer then provided the base pressure differential from that level throughout the α -sweep. Approximately 97 percent of the test data was obtained using the continuous sweep mode of operation.

3.3 DATA UNCERTAINTY

An evaluation of the influence of random measurement errors is presented in this section to provide a partial measure of the uncertainty of the final test results presented in this report. Although evaluation of the systematic measurement error (bias) is not included, it should be noted that the instrumentation precision values (given in Section 2.3) used in this evaluation represent a total uncertainty combination of both systematic and two-sigma random error contributions.

3.3.1 Test Conditions

Uncertainties in the basic tunnel parameters P_o and T_o (see Section 2.3) and the two-sigma deviation in Mach number determined from test section flow calibrations were used to estimate uncertainties in the other free-stream properties, using the Taylor series method of error propagation.

Uncertainty (\pm), percent						
M_∞	M_∞	P_o	T_o	p_∞	q_∞	Re_d
1.50	1.3	0.2	0.5	2.9	0.3	0.9
2.00	1.0	↓	↓	3.1	1.1	1.2
2.50	0.8			3.1	1.5	1.3
3.01	0.7			3.2	1.8	1.4
3.47	0.6			2.9	1.7	1.3
4.02	0.5			2.7	1.7	1.3
4.50	0.4			2.5	1.6	1.3

3.3.2 Test Data

The data are presented in the body-axis system. Pitching moments are referenced to a point on the model longitudinal centerline at the nose-body juncture (see Fig. 4). The model base diameter is used as the reference length and the body cross-sectional area is the reference area for all aerodynamic coefficients.

The balance and base pressure uncertainties listed in Section 2.3 were combined with uncertainties in the tunnel parameters, using the Taylor series method of error propagation, to estimate the uncertainty of the aerodynamic coefficients, and these are presented below. Results shown are from the first entry. Those from the second entry are generally somewhat lower.

Absolute Uncertainty (\pm) Near Maximum Measured Coefficient Value				
M_∞	C_N	C_m	C_{A_t}	C_A
1.50	0.017	0.085	0.007	0.021
2.00	0.028	0.120	0.013	0.022

M_∞	C_N	C_m	C_{A_t}	C_A
2.50	0.036	0.115	0.011	0.015
3.01	0.046	0.184	0.020	0.023
3.47	0.034	0.061	0.012	0.014
4.02	0.044	0.174	0.021	0.022
4.50	0.038	0.075	0.015	0.015

The basic precision of the aerodynamic coefficients was also computed using only the balance and base pressure uncertainties listed in Section 2.3 along with the nominal test conditions, using the assumption that the free-stream flow nonuniformity is a bias type of uncertainty which is constant for all test runs. These values, therefore, represent the data repeatability expected and are especially useful for detailed discrimination purposes in parametric model studies.

Repeatability (\pm)
Measured Coefficient Value

M_∞	C_N	C_m	C_{A_t}	C_A
1.50	0.016	0.080	0.006	0.020
2.00	0.016	0.083	0.007	0.014
2.50	0.018	0.074	0.007	0.013
3.01	0.020	0.101	0.008	0.010
3.47	0.023	0.049	0.009	0.012
4.02	0.028	0.140	0.011	0.012
4.50	0.032	0.068	0.013	0.014

The uncertainty in model angle of attack (α), as determined from tunnel sector calibrations and consideration of the possible errors in model deflection calculations, is estimated to be ± 0.1 deg.

4.0 RESULTS AND DISCUSSION

Results are presented from generalized nose configurations which illustrate typical effects of nose bluntness, nose and afterbody caliber, and Mach number on the body aerodynamic force and moment characteristics. A nose family consists of a group of noses having the same virtual length (caliber) and ogive radius with varying bluntness (R_N/R_B). Results are also shown for two power-series nose configurations of particular

interest to the test sponsors, and selected results are compared to theoretical solutions of forebody axial force at zero model pitch (C_{A_0}). For these solutions, which were performed at AEDC-VKF, skin-friction drag was obtained using a method based on the work of Patankar and Spalding (Ref. 2) as modified by Mayne and Dyer (Ref. 3). Pressure drag data were obtained from calculations made using the methods of Inouye, Rakich, and Lomax (Ref. 4).

An indication that laminar flow was maintained throughout the test near $\alpha = 0$ is shown in Figure 6. The forebody axial-force coefficient, C_{A_0} , for the sharp nose (N22) configuration remains very near the laminar level at the lowest Mach number ($M_\infty = 1.50$), even with the longest configuration tested. Transition Reynolds number increases with Mach number and as this test was conducted at a constant unit Reynolds number, it is believed that the laminar flow criteria for all results at $\alpha = 0$ were met.

Nose geometry effects are presented in Figs. 7 through 11. The 3-caliber family of noses with the 10-caliber afterbody at Mach numbers 1.50 and 3.01 (Fig. 7) was selected to illustrate the effects of hemispherical nose bluntness. The results for the 2- and 4-caliber nose families were very similar, although of different magnitudes. Little measurable effect on the normal-force (C_N) or pitching-moment (C_m) coefficients was observed at Mach 1.50. Forebody axial-force coefficient (C_A) increased nonlinearly with bluntness. At Mach 3.01 the same trend existed in C_A , but C_N decreased somewhat with increased bluntness. The center of pressure measured in calibers aft of the nose-body juncture (XCP) moved rearward at $M_\infty = 3.01$ with increases in nose bluntness. All XCP results between -2 and 2-deg angle of attack are omitted since the calculation of this parameter ($-C_m/C_N$) produces unrealistic values near a C_N of zero. Furthermore, values of XCP at $\alpha = 0$ obtained from C_{m_a}/C_{N_a} are also omitted for $M_\infty = 1.50$ and 2.0 in most cases because of the flatness of the C_m curve through $\alpha = 0$, coupled with the uncertainty in measurement of C_m (see Sect. 3.3.2).

A comparison of the theoretical C_{A_0} solutions with results for nose bluntness variation is given in Fig. 8 for the 3-caliber nose family and 10-caliber afterbody combination. Generally good agreement can be seen for low and moderate bluntnesses with some difference at 0.75 bluntness at Mach 3.01. The curves reflect a parabolic increase in C_{A_0} with nose bluntness, principally caused by pressure drag increases.

The nose shape effects on the 2.25-caliber nose family and the two power-series noses with the 10-caliber afterbody are presented in Figs. 9 and 10, respectively, for Mach 3.01. The 2.25-caliber nose family exhibited the same general trends discussed above. The two power-series noses were nearly identical in C_N and C_m across the angle-of-attack range; therefore, XCP behaved similarly. The blunter N31 configuration, however, had a 50-percent higher forebody drag (C_A) over the angle-of-attack range.

The nose caliber effect for sharp and 50-percent blunt nose geometries is illustrated in Fig. 11 for Mach 3.01. A 1-caliber, 50-percent blunt nose was not tested, so only 2-, 3-, and 4-caliber nose configurations are presented in Fig. 11b. The C_N increase at a given attitude with nose caliber increase was considerably more pronounced on the sharp nose shapes than on the blunt configurations. The XCP moved about 0.5 calibers forward with each 1-caliber increase in nose length. The variation in C_A resembled a nose-bluntness effect with decreasing nose caliber corresponding to increasing nose bluntness. Results from the noses of intermediate caliber are omitted for figure clarity but could be interpolated from the results shown. The trends are similar at other Mach numbers.

The remaining configuration variable examined was afterbody length (the midbody-afterbody combination is referred to as an afterbody). This effect is shown in Fig. 12 for Mach 3.01. The results for 3-caliber sharp and blunt noses (N18 and N20, respectively) given in Fig. 12 typify most of the data. The slight increase in C_A as the afterbody is lengthened results from the increase in skin-friction drag. The changes in C_N and C_m are almost linear with afterbody length at a given attitude, and the incremental change is about the same for both nose shapes. Predictably, XCP moves aft with afterbody length increases, with close to a 0.8-caliber shift for a 2-caliber afterbody change at the higher angles of attack for both nose configurations.

Mach number effects are presented in Figs. 13 through 17. Again, the 3-caliber noses are presented as typical of all the nose families. These noses, with the 10-caliber afterbody, are shown in Figs. 13 and 14. Except at high angles of attack, the XCP results (Fig. 13) show little change between Mach 1.50 and 2.00 and between Mach 3.01 and 4.02. The center of pressure generally moves aft as Mach number increases. Slopes of the C_N data (at $\alpha = 0$) for the blunt noses are such that C_{N_α} increases from Mach 1.50 to a maximum near Mach 3.0 and then decreases with further Mach number increases (Fig. 14). For the sharp nose configuration (N18*M9*A17), C_{N_α} increases with Mach number increase. Increasing Mach number generally produced a more negative C_{m_α} , with little change in C_{m_α} caused by bluntness except at $M_\infty = 3.01$ where the sharp nose configuration departed from the general trend. For noses of 25-percent bluntness or less, C_A or C_{A_0} shows little variation with Mach number. For noses of greater bluntness there was an increase in C_A or C_{A_0} with increased Mach number which leveled off at the higher Mach numbers. Included in Fig. 14 are results of the theoretical laminar flow C_{A_0} calculations for Mach number variation on the N18 and N20 noses with the 10-caliber afterbody. The results show particularly good agreement between experiment and theory at Mach 4.02 for both configurations and at Mach 1.50 for the N18 configuration.

Mach number effects for the power-series noses with 10-caliber afterbody configurations are given in Figs. 15 and 16. The data trends with Mach number for these

noses are very similar to those noted for the 3.0-caliber noses. The value of C_{A_0} is higher for the blunter (N31) configurations except at Mach 1.50 where C_{A_0} was about the same for both configurations (see Fig. 16).

Comparisons of the supersonic results from this test program with subsonic and transonic results of C_{N_α} , C_{m_α} , and C_{A_0} obtained on the same models in two other test programs (Refs. 5 and 6), are given in Fig. 17 for the hemisphere-cylinder nose (N10) and the sharp 4-caliber nose (N22), both on the 10-caliber afterbody. The results are fairly consistent across the Mach number range particularly in C_{N_α} and C_{A_0} . The data indicate an abrupt change in C_{m_α} between $M_\infty \sim 1.2$ and 1.5. The reason for this change is not known. However, there is reasonable agreement between the present data for the N22 configuration at $M_\infty = 1.5$ with results from Ref. 6. The small differences in the coefficients between the two tests, particularly in C_{A_0} , could be a Reynolds number effect. The Reynolds number, Re_d , was about 0.50 million in the tests of Ref. 6 and 0.18 million in this test.

5.0 SUMMARY OF RESULTS

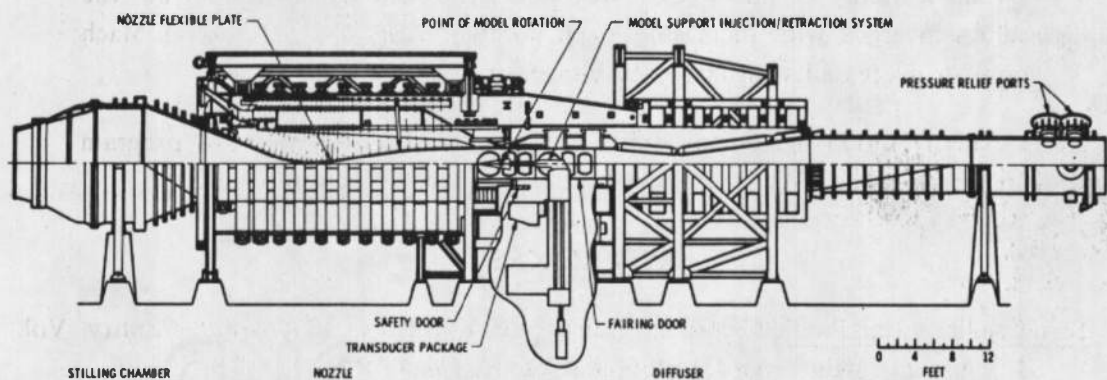
A static force test was conducted on a number of nose and cylindrical afterbody configurations at Mach numbers from 1.5 to 4.5 at angles of attack up to 14 deg. The test Reynolds number, based on model diameter, was 0.18 million and was chosen to ensure a laminar boundary-layer condition on the models at $\alpha = 0$. Results of the test are summarized as follows:

1. Generally, good agreement was obtained with analytical solutions for C_{A_0} for a laminar flow condition.
2. Increases in Mach number generally resulted in a rearward movement of the center of pressure.
3. For nose geometries with 25-percent bluntness or less, C_{A_0} remained constant or decreased slightly with increasing Mach number. Noses of greater bluntness exhibited an increase in C_{A_0} with Mach number.
4. Typically, nose caliber increases moved the center of pressure forward and decreased C_{A_0} parabolically.
5. Lengthening of the afterbody caused little change in C_A and linear increases in C_N and C_m with a corresponding rearward movement in center of pressure at a given α .

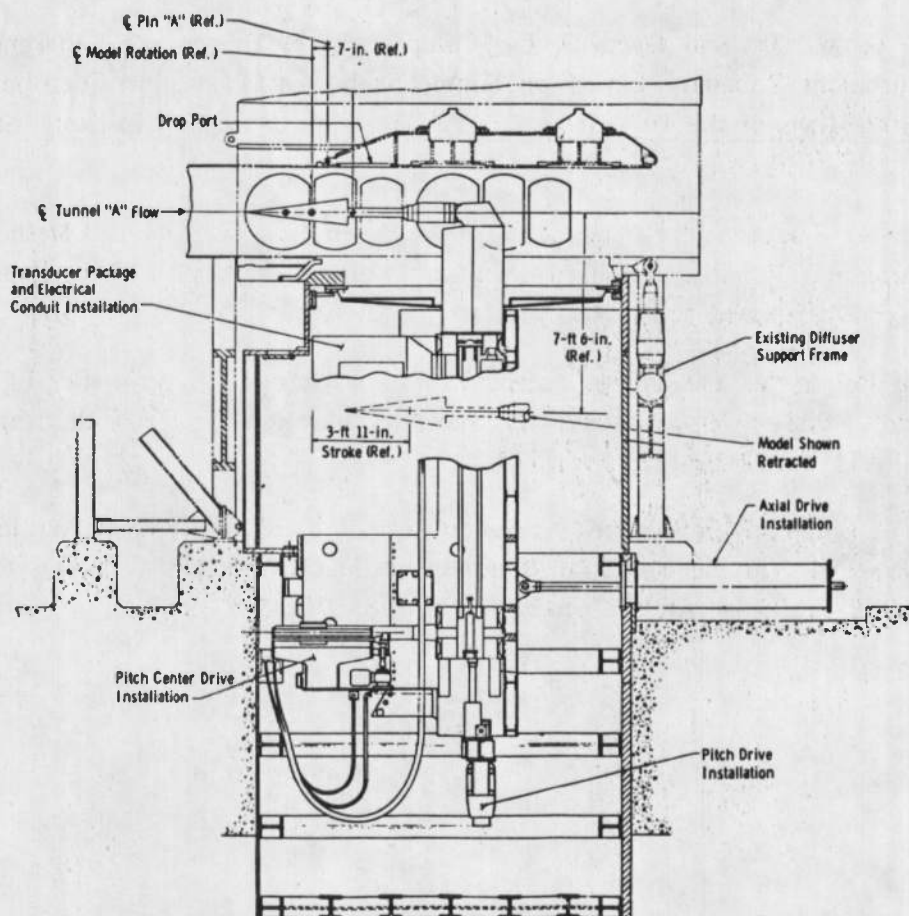
6. Within a family of noses, C_{N_a} was about the same at Mach 1.50, but the values diverged with increasing Mach number. Also, C_{N_a} at a given Mach number decreased with increased bluntness.
7. Generally, good agreement exists between results from this test program and from other tests on the same models at lower Mach numbers.

REFERENCES

1. Test Facilities Handbook (Tenth Edition). "von Kármán Gas Dynamics Facility, Vol. 3." Arnold Engineering Development Center, May 1974.
2. Patankar, S. V. and Spalding, D. B. Heat and Mass Transfer in Boundary Layers. CRC Press, Cleveland, 1968.
3. Mayne, A. W., Jr., and Dyer, D. F. "Comparisons of Theory and Experiment for Turbulent Boundary Layers on Simple Shapes at Hypersonic Conditions." in Proceedings of the 1970 Heat Transfer and Fluid Mechanics Institute, Stanford University Press, 1970, pp. 168-188.
4. Inouye, M., Rakich, J. V., and Lomax, H. "A Description of Numerical Methods and Computer Programs for Two-Dimensional and Axisymmetric Supersonic Flow over Blunt-Nosed and Flared Bodies." NASA-TN D-2970, August 1965.
5. Rogers, Robert M. and Bulter, Carroll B. "Aerodynamic Characteristics of several Bluff Body Configurations at Subsonic and Transonic Mach Numbers." AFATL-TR-72-25, February 1972.
6. Allee, E. G., Jr. "Aerodynamic Characteristics of Two Bodies of Revolution with Noses of Varying Spherical Bluntness at Mach Numbers from 0.6 to 1.5." AEDC-TR-73-44, AFATL-TR-73-50 (AD758817), April 1973.



a. VKF Tunnel A



b. Model injection system

Figure 1. Wind tunnel and model injection system.

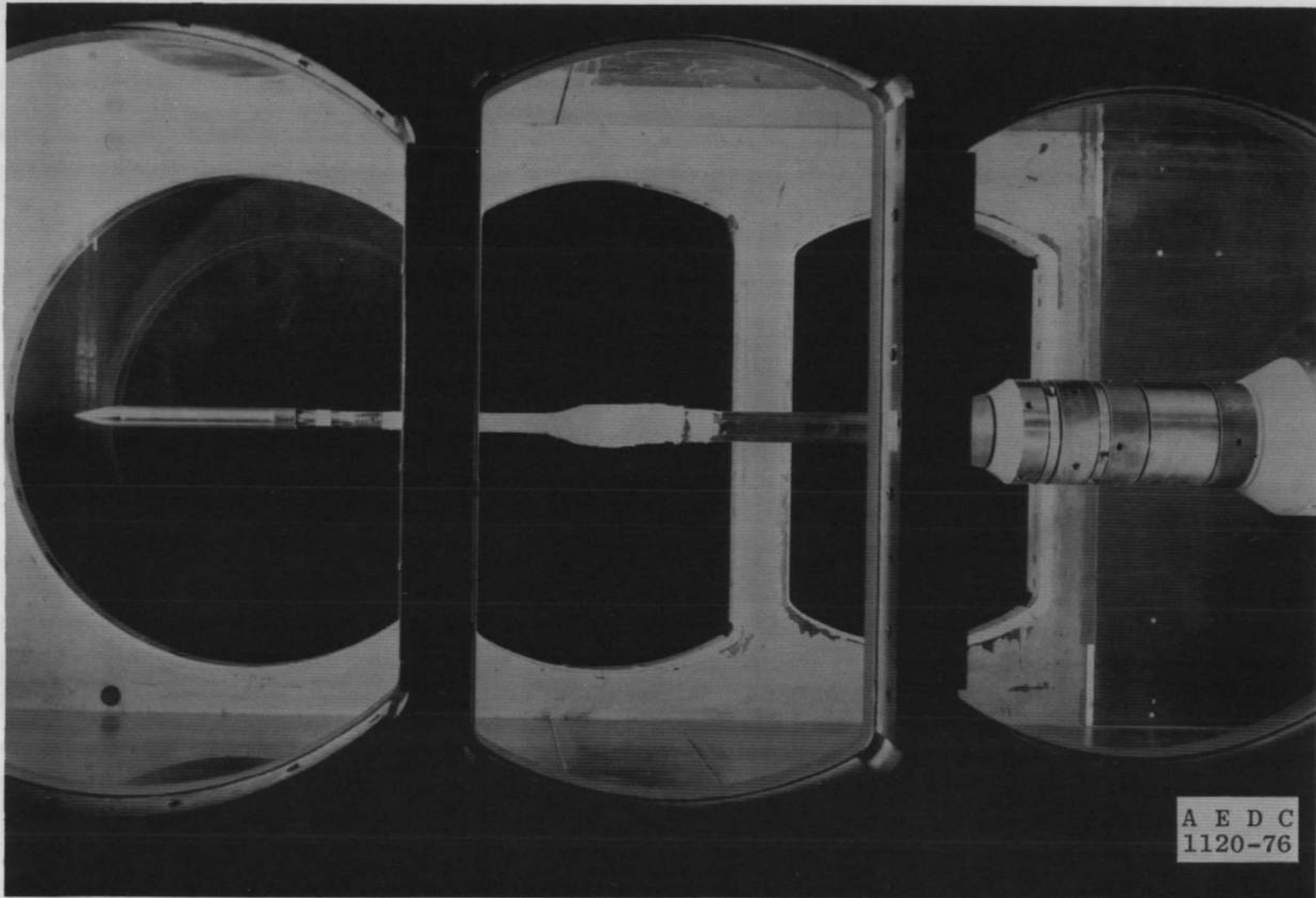
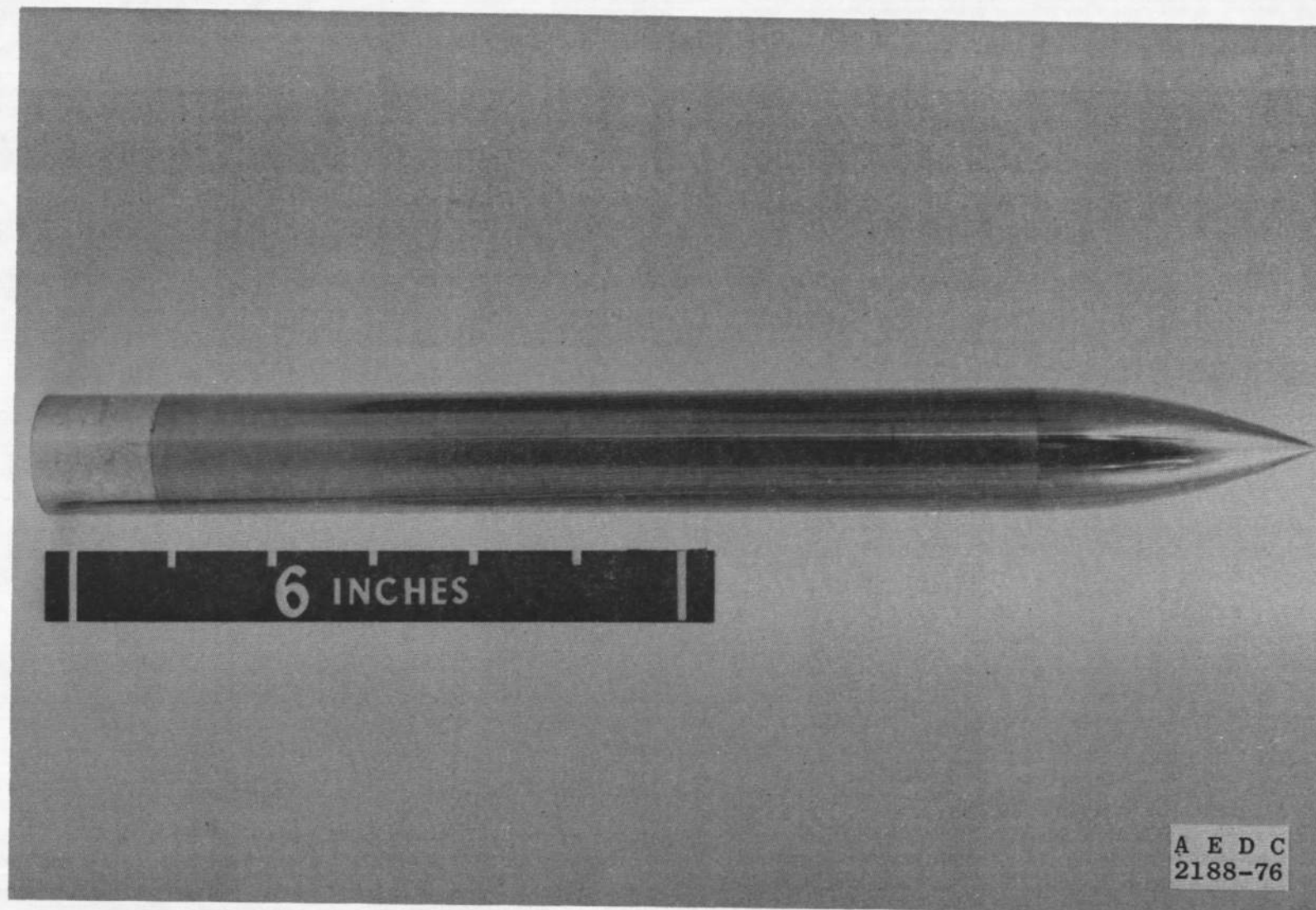
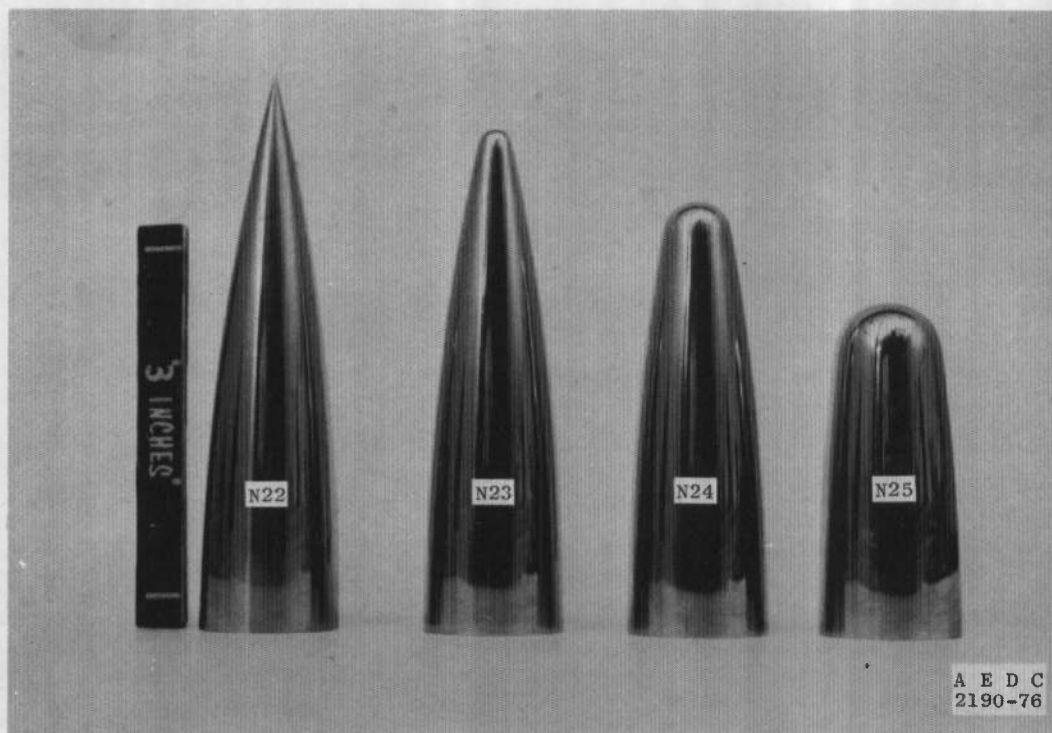


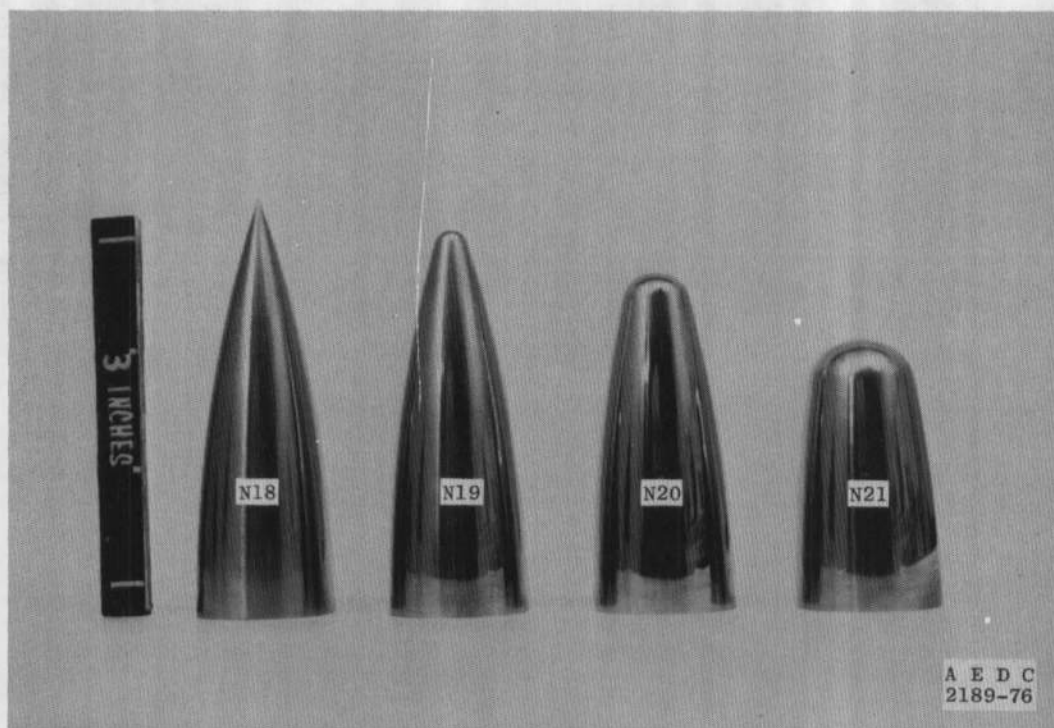
Figure 2. Model installation in Tunnel A.



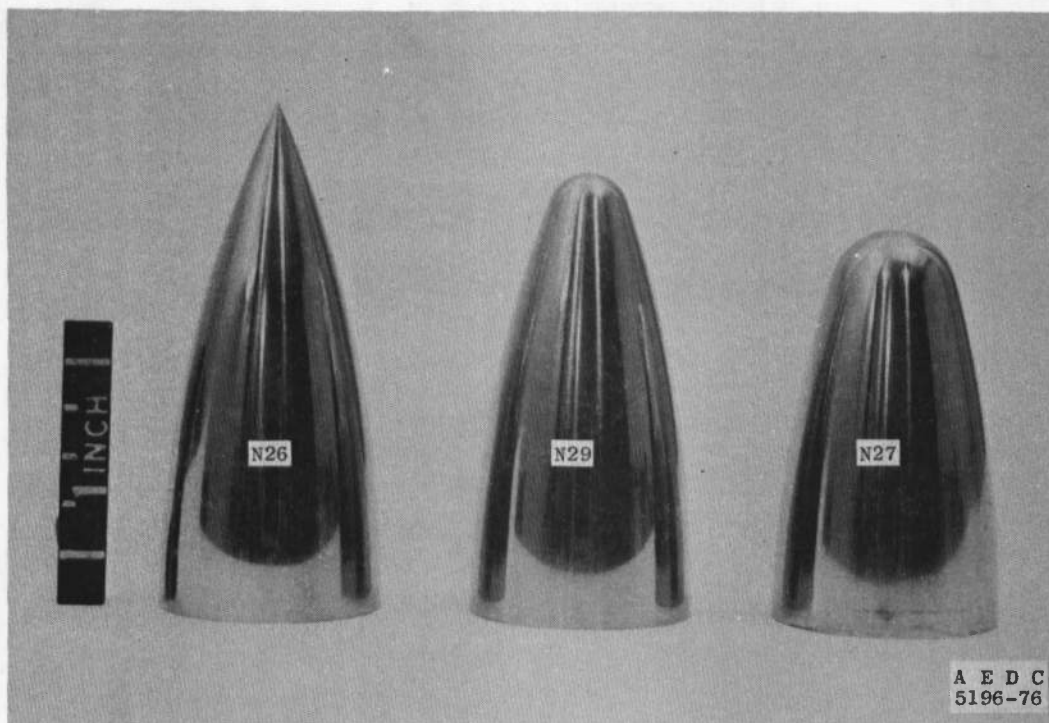
a. Typical configuration, N26*M7*A17
Figure 3. Photographs of model and components.



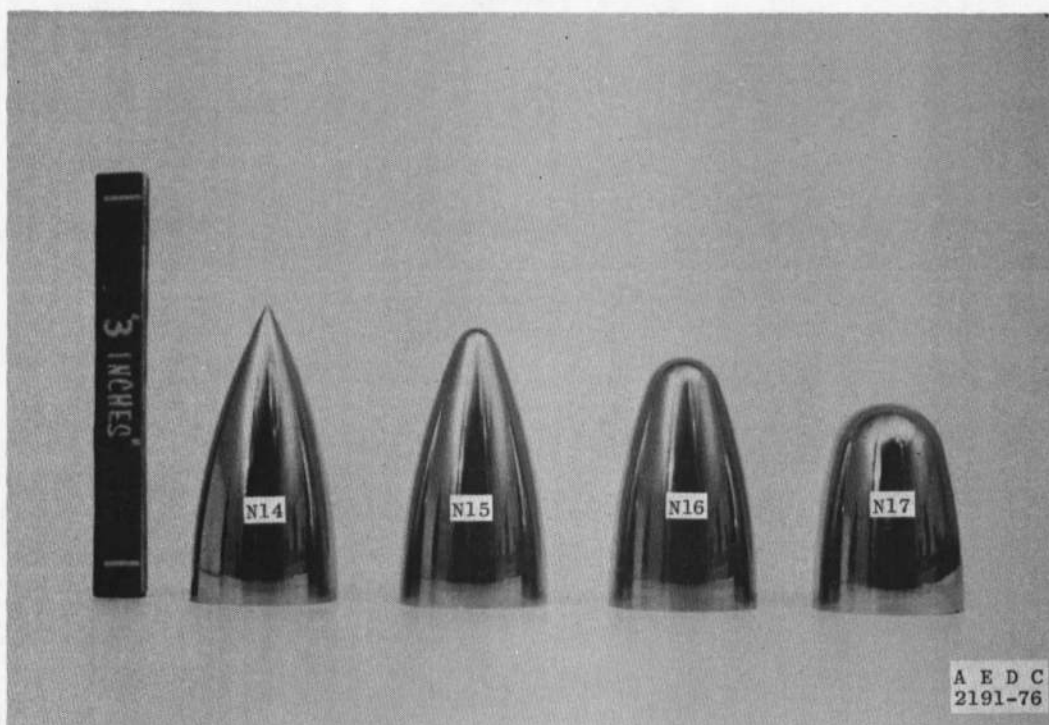
b. 4.0-caliber noses



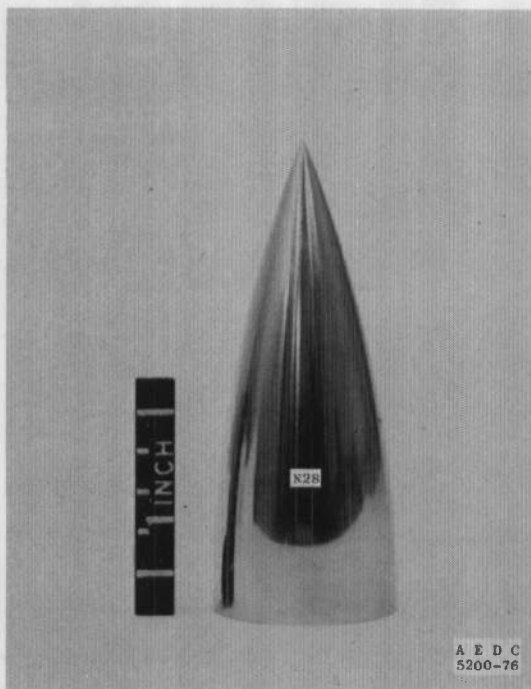
c. 3.0-caliber noses
Figure 3. Continued.



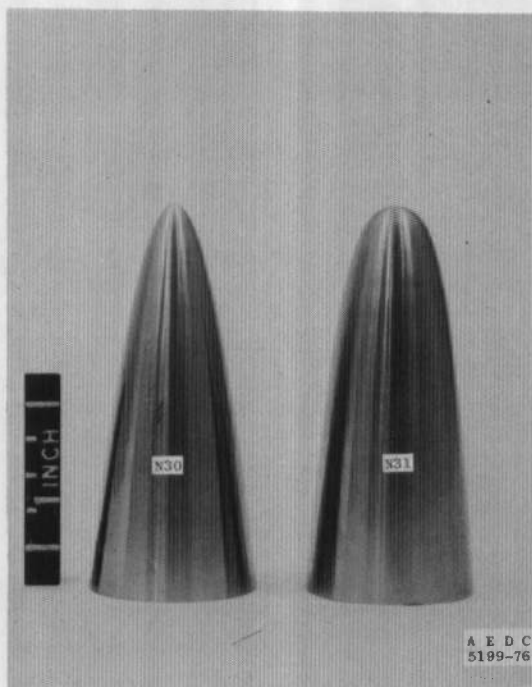
d. 2.25-caliber noses



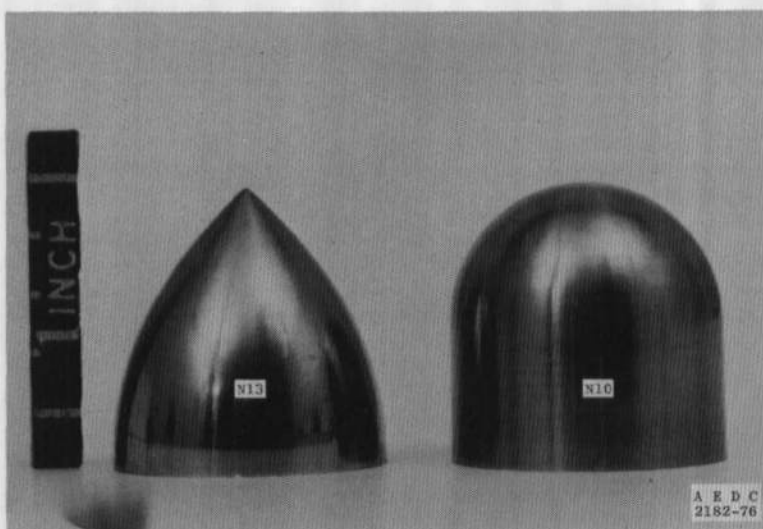
e. 2.0-caliber noses
Figure 3. Continued.



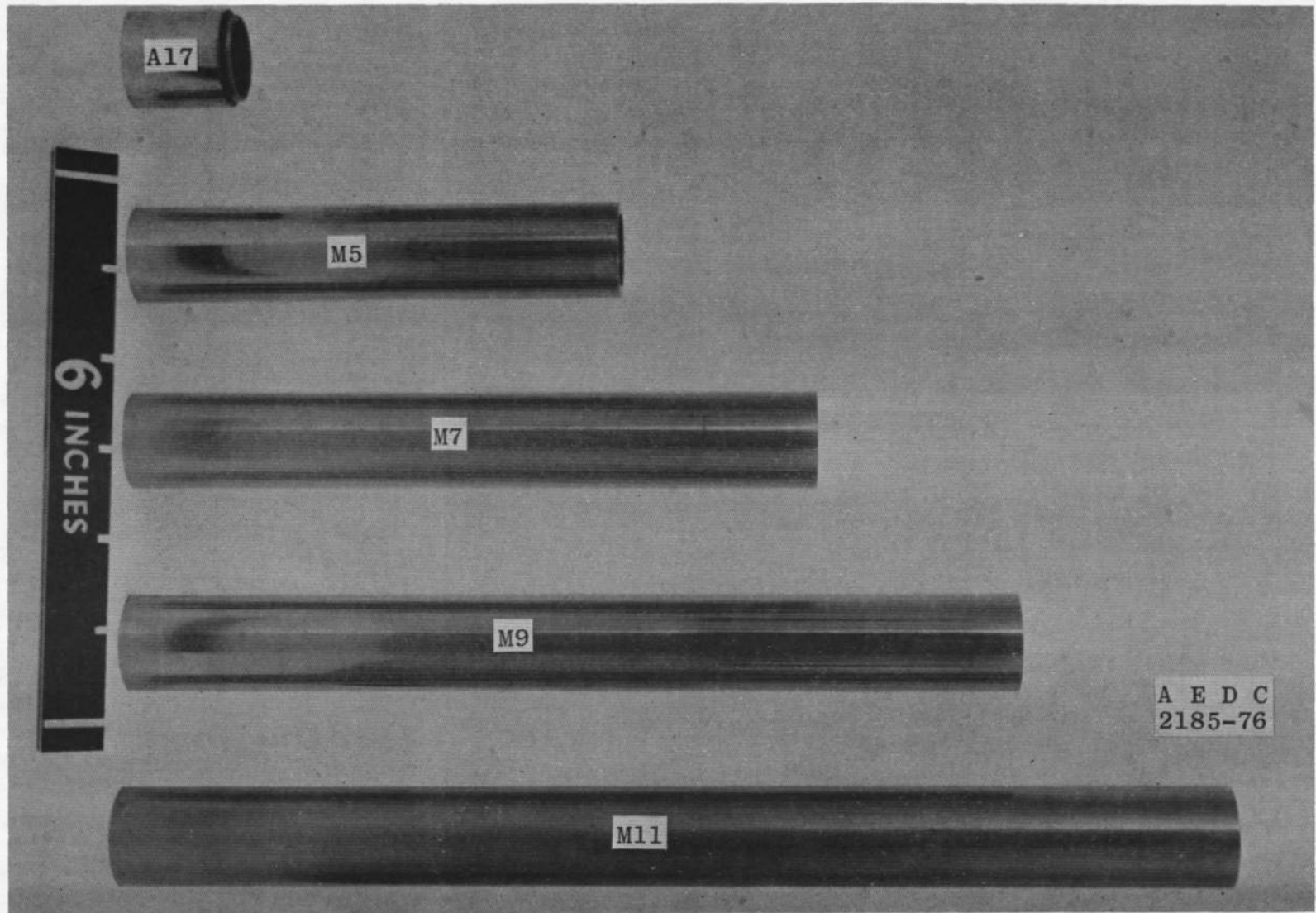
f. 2.5-caliber nose



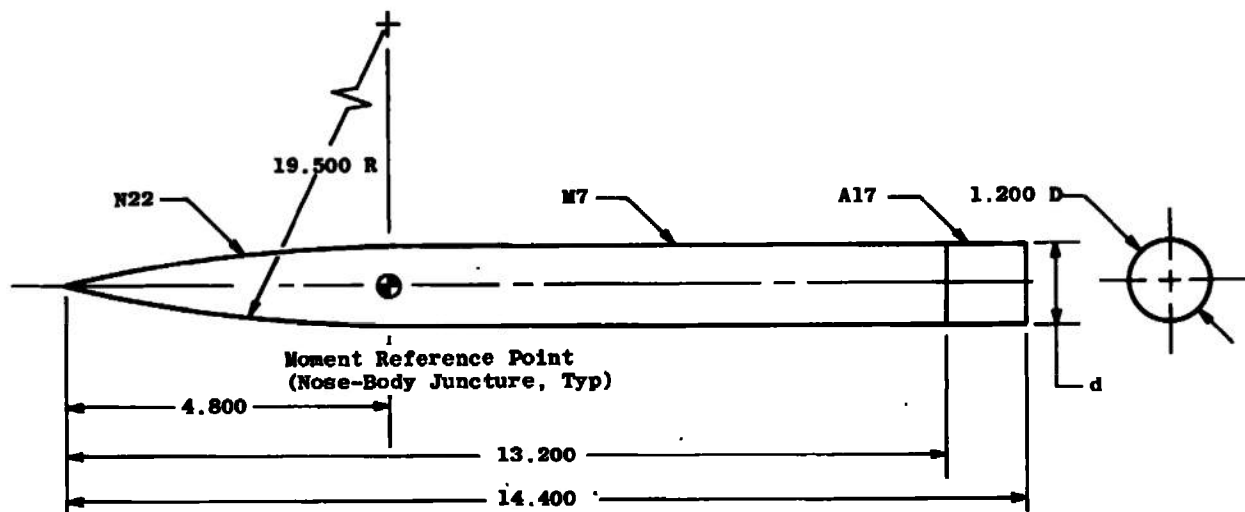
g. Power-series noses



h. 1.0-caliber noses
Figure 3. Continued.



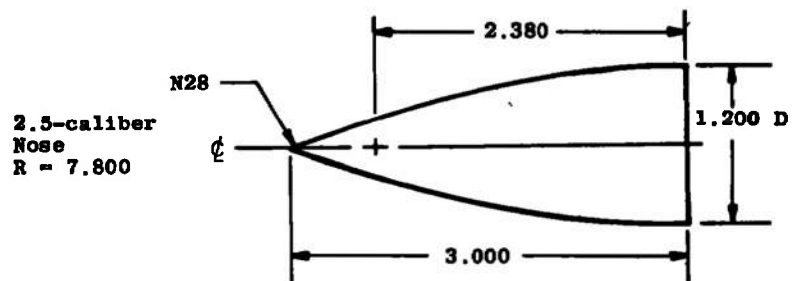
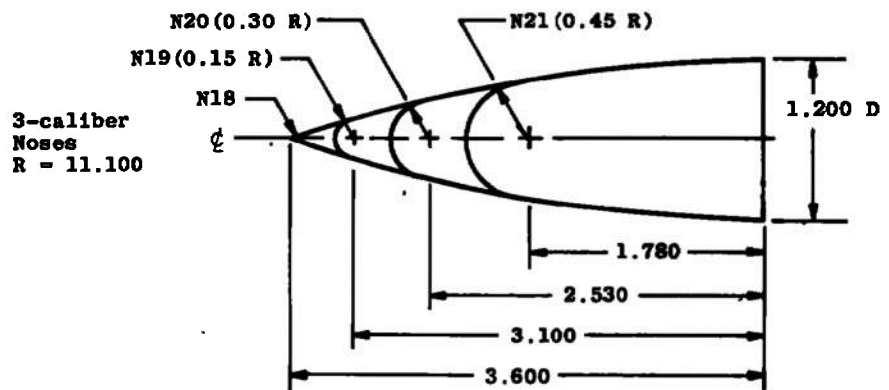
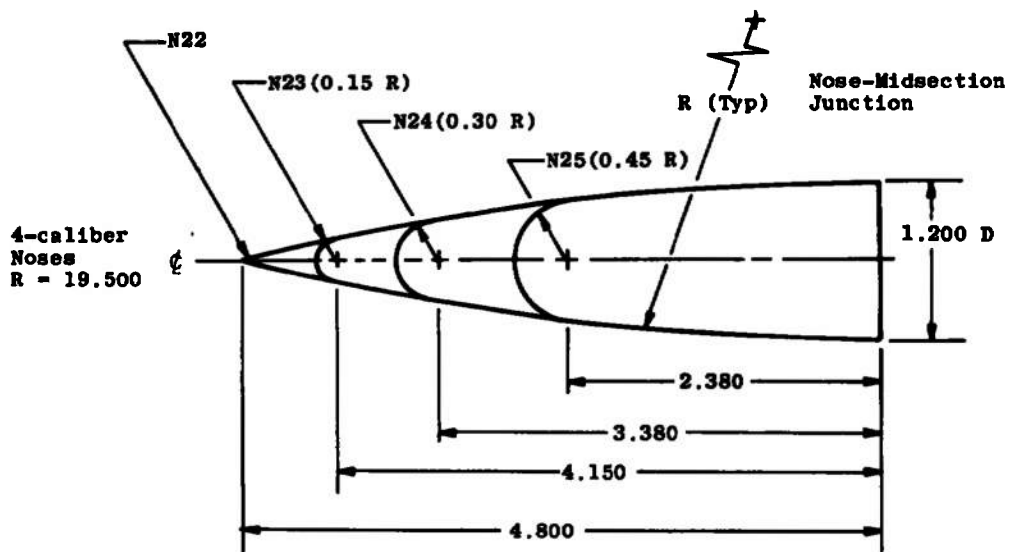
i. Midbodies and afterbody
Figure 3. Concluded.



All Dimensions in Inches

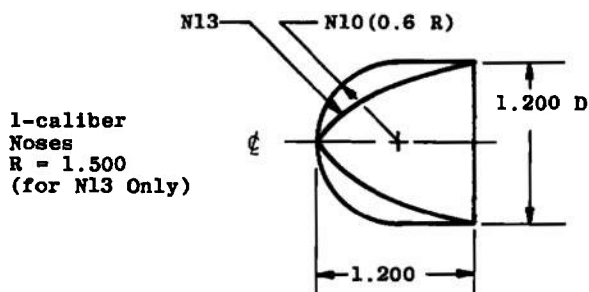
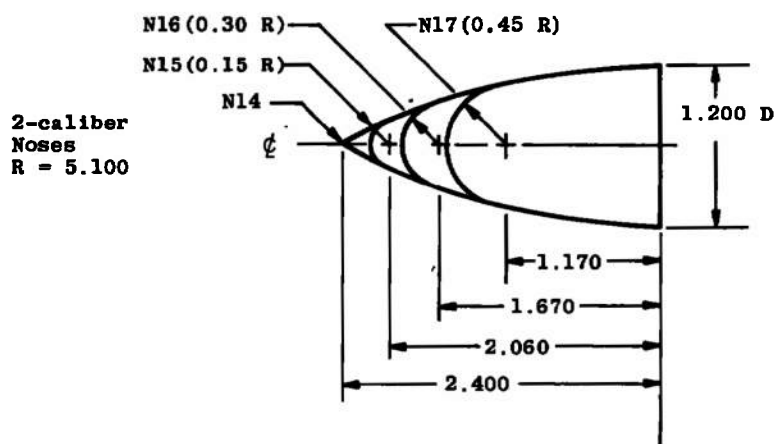
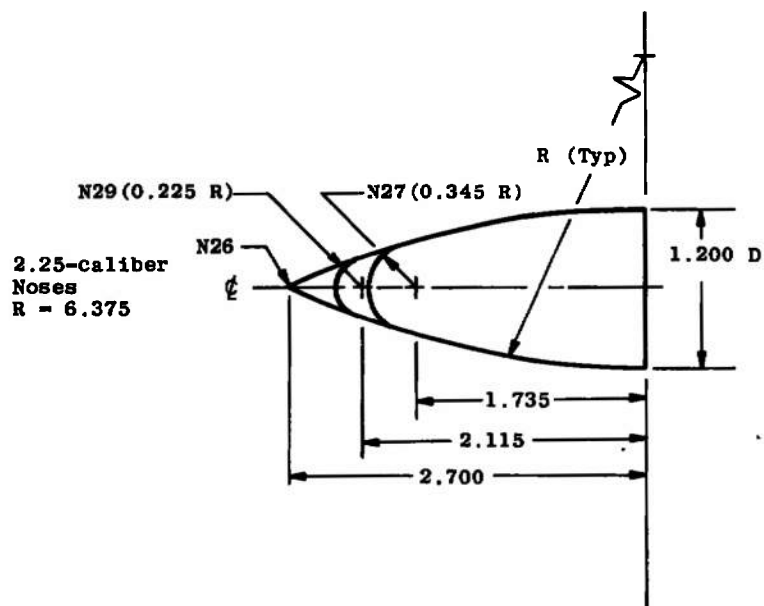
a. Typical configuration, N22*M7*A17

Figure 4. Model details.



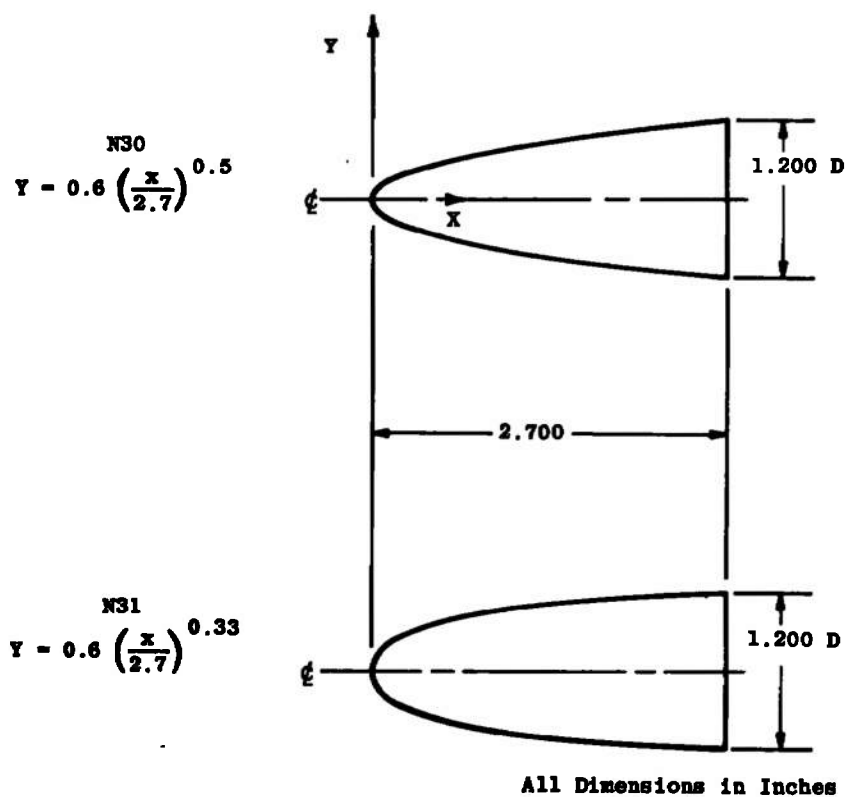
All Dimensions in Inches

b. Nose sections of 2.5, 3.0, and 4.0 caliber
Figure 4. Continued.

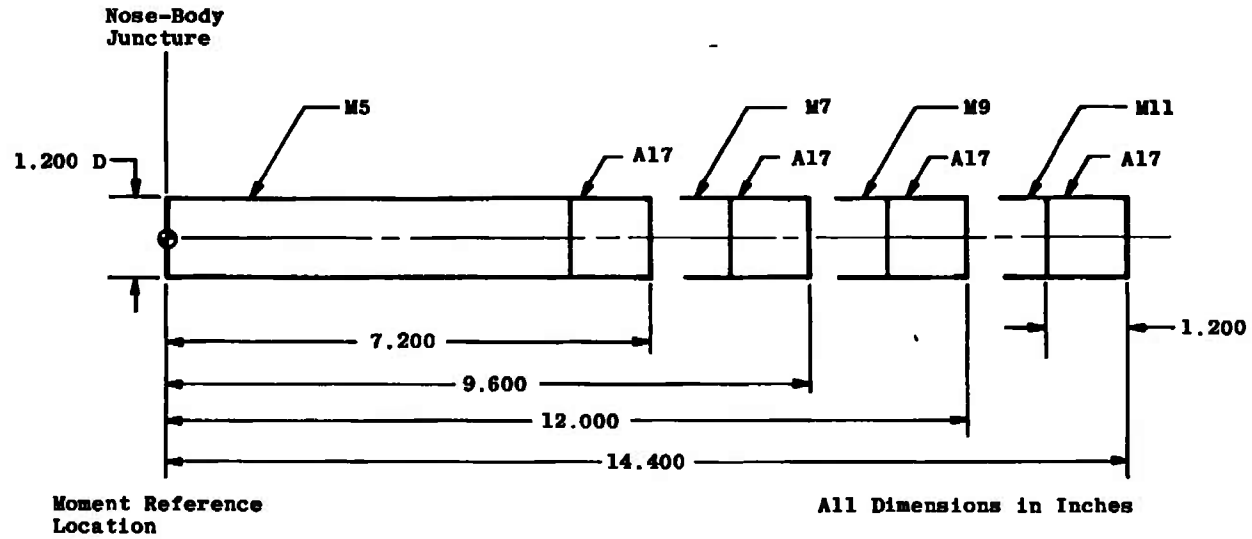


All Dimensions in Inches

c. Nose sections of 1.0, 2.0, and 2.25 caliber
Figure 4. Continued.



d. Power-series nose sections
Figure 4. Continued.



e. Midbody and afterbody sections
Figure 4. Concluded.

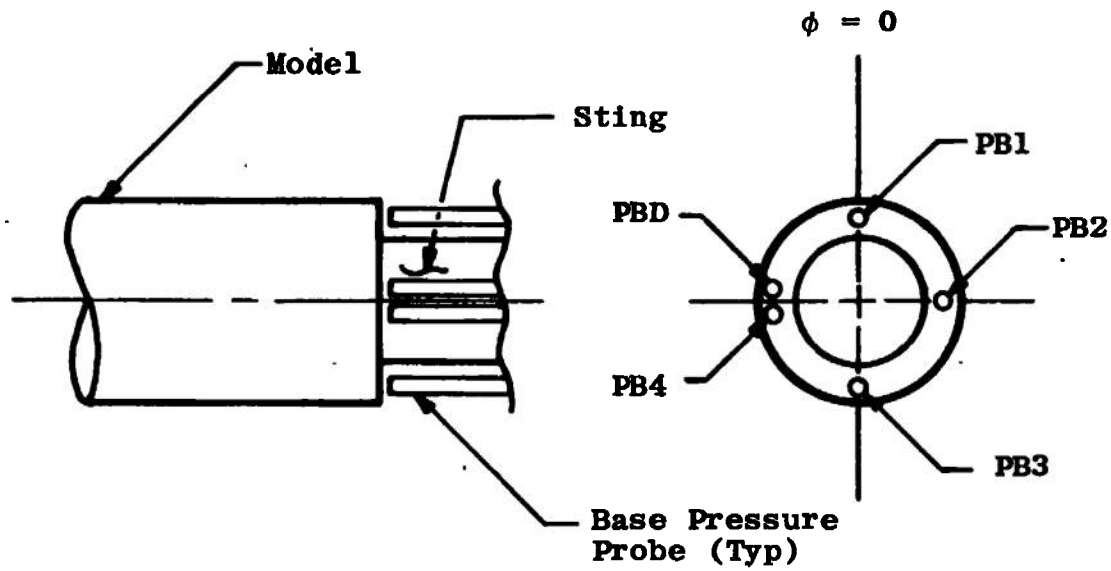


Figure 5. Base pressure probe orientation.

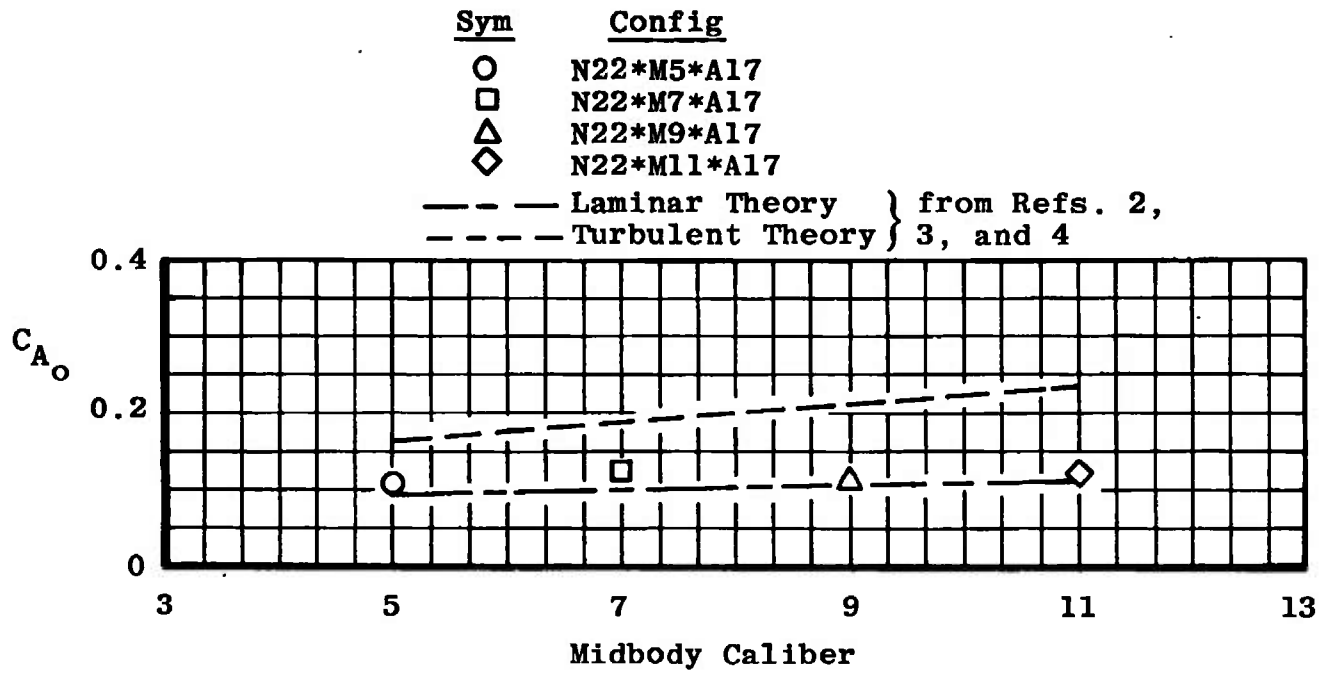
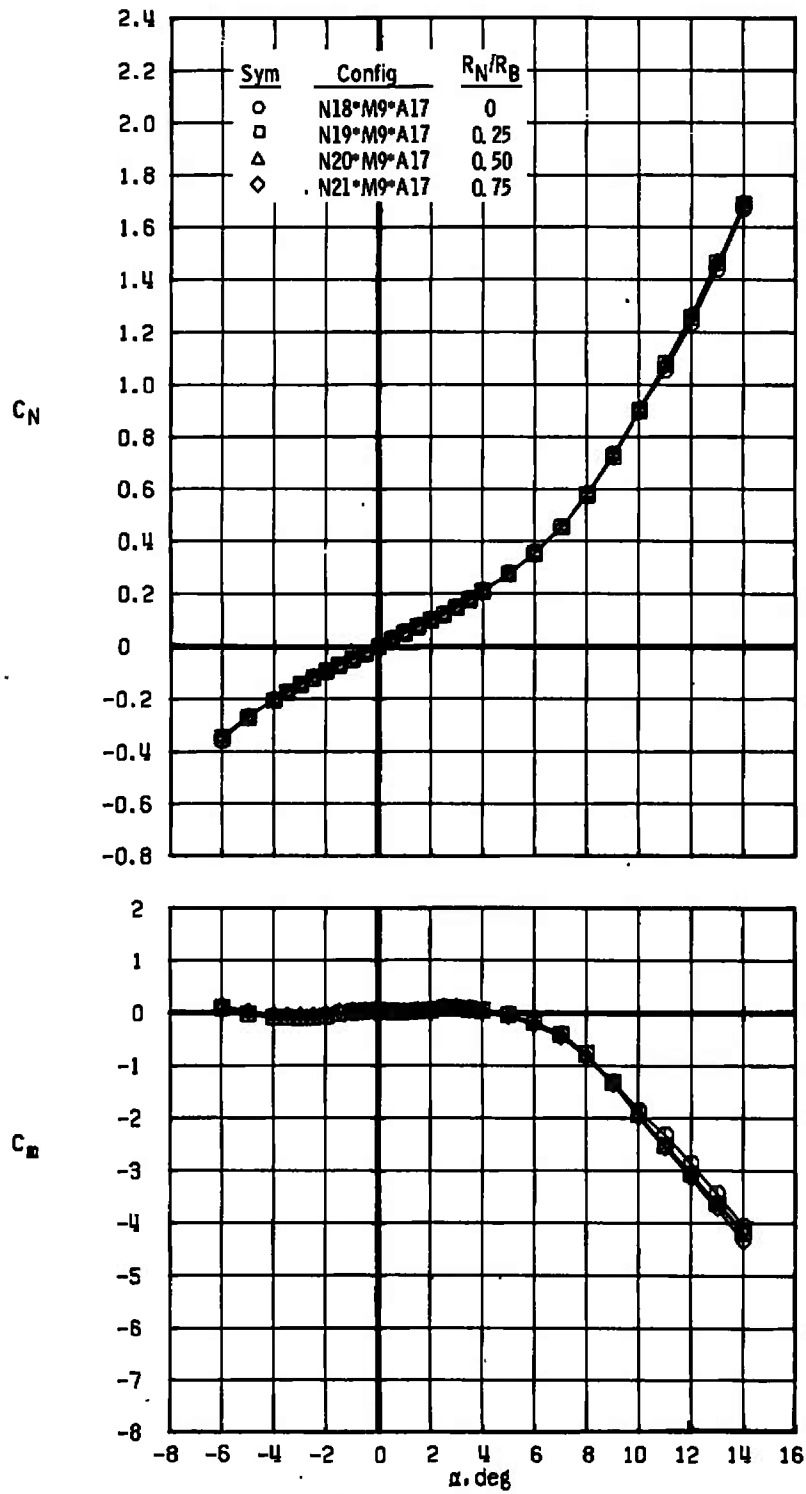
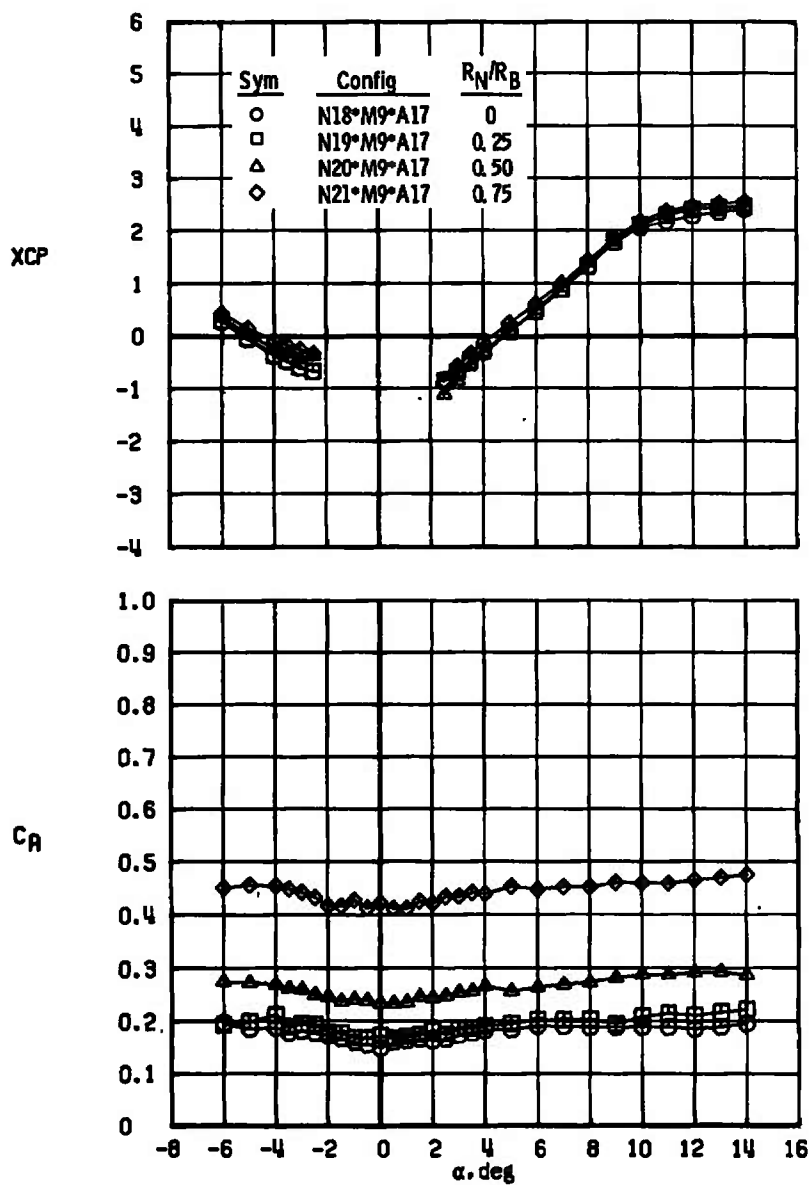


Figure 6. Comparison of experimental and theoretical C_{A0} for variations in midbody caliber at $M_\infty = 1.50$.



a. $M_\infty = 1.50$
Figure 7. Effect of nose bluntness on force and moment characteristics of the 3.0-caliber nose configurations.



a. Concluded
Figure 7. Continued.

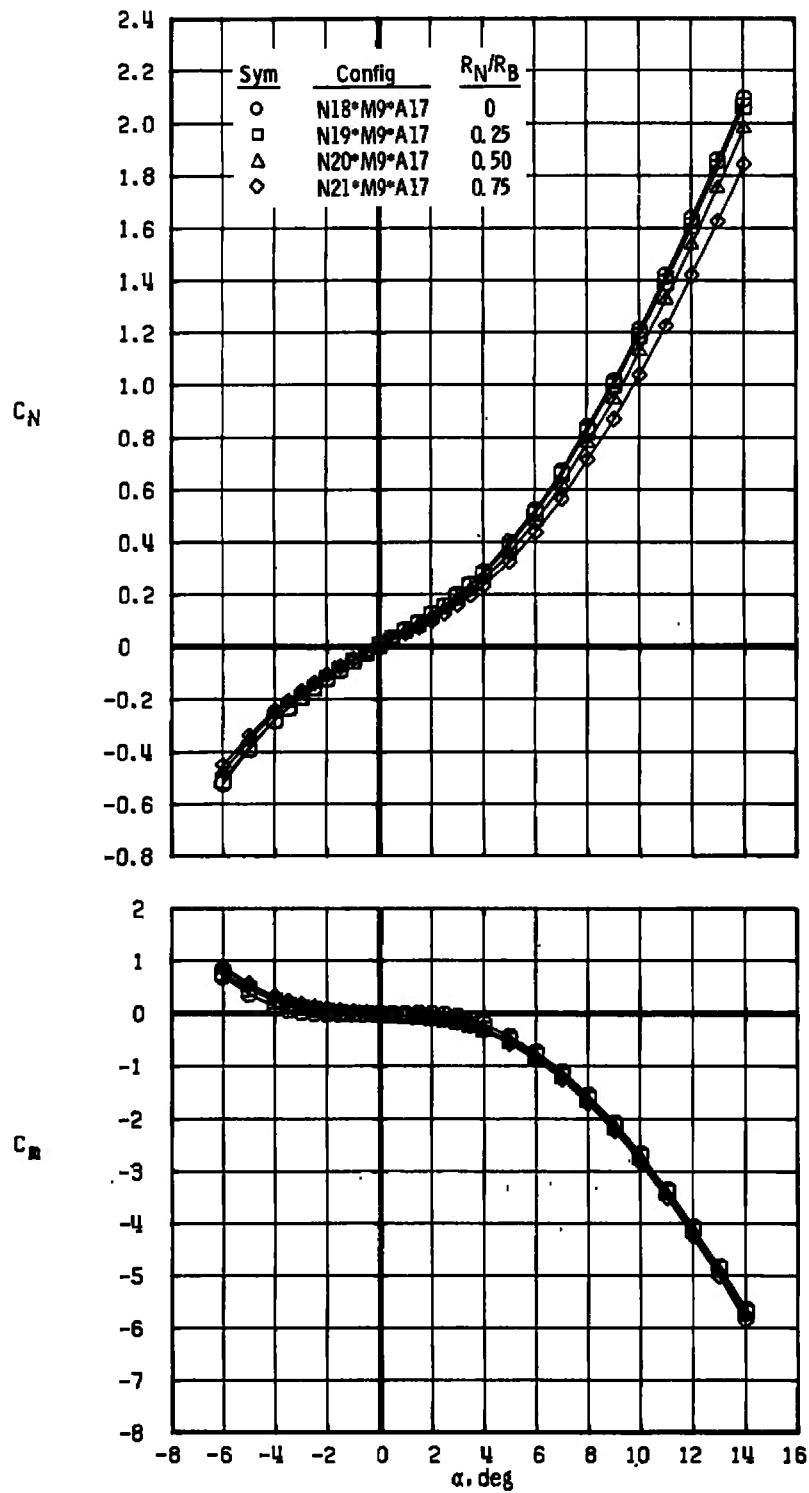
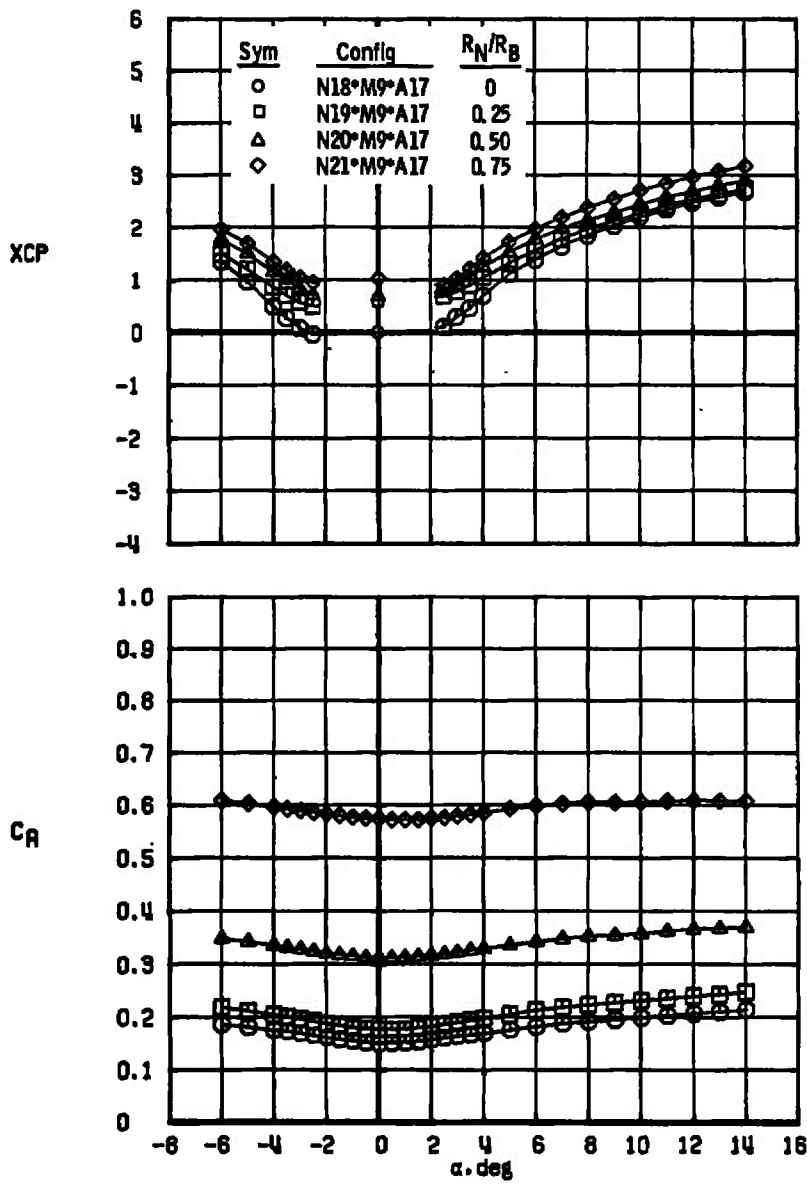


Figure 7. Continued.



b. Concluded
Figure 7. Concluded.

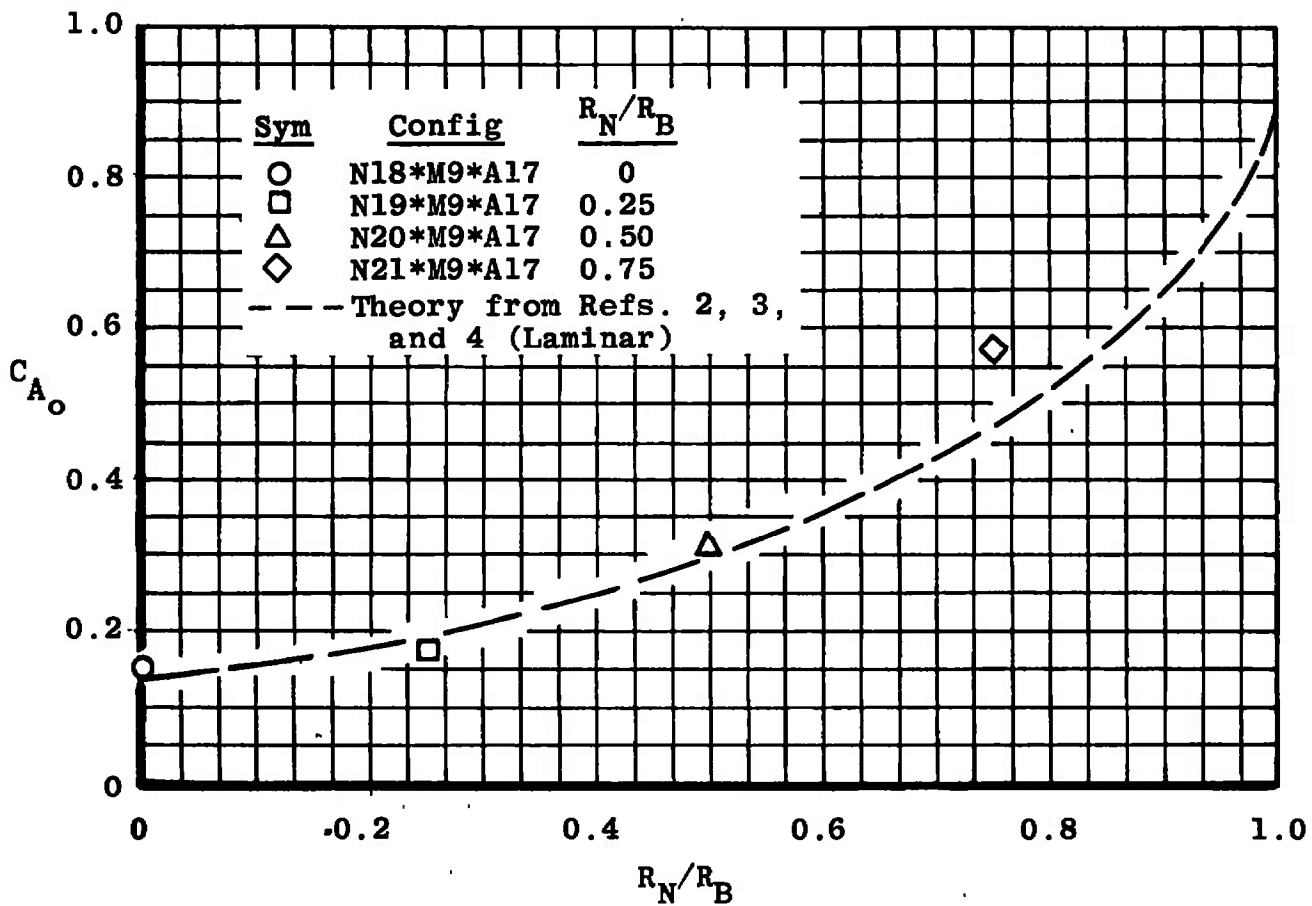


Figure 8. Comparison of experimental and theoretical C_{A_0} for variations in nose bluntness for the 3.0-caliber configurations, $M_\infty = 3.01$.

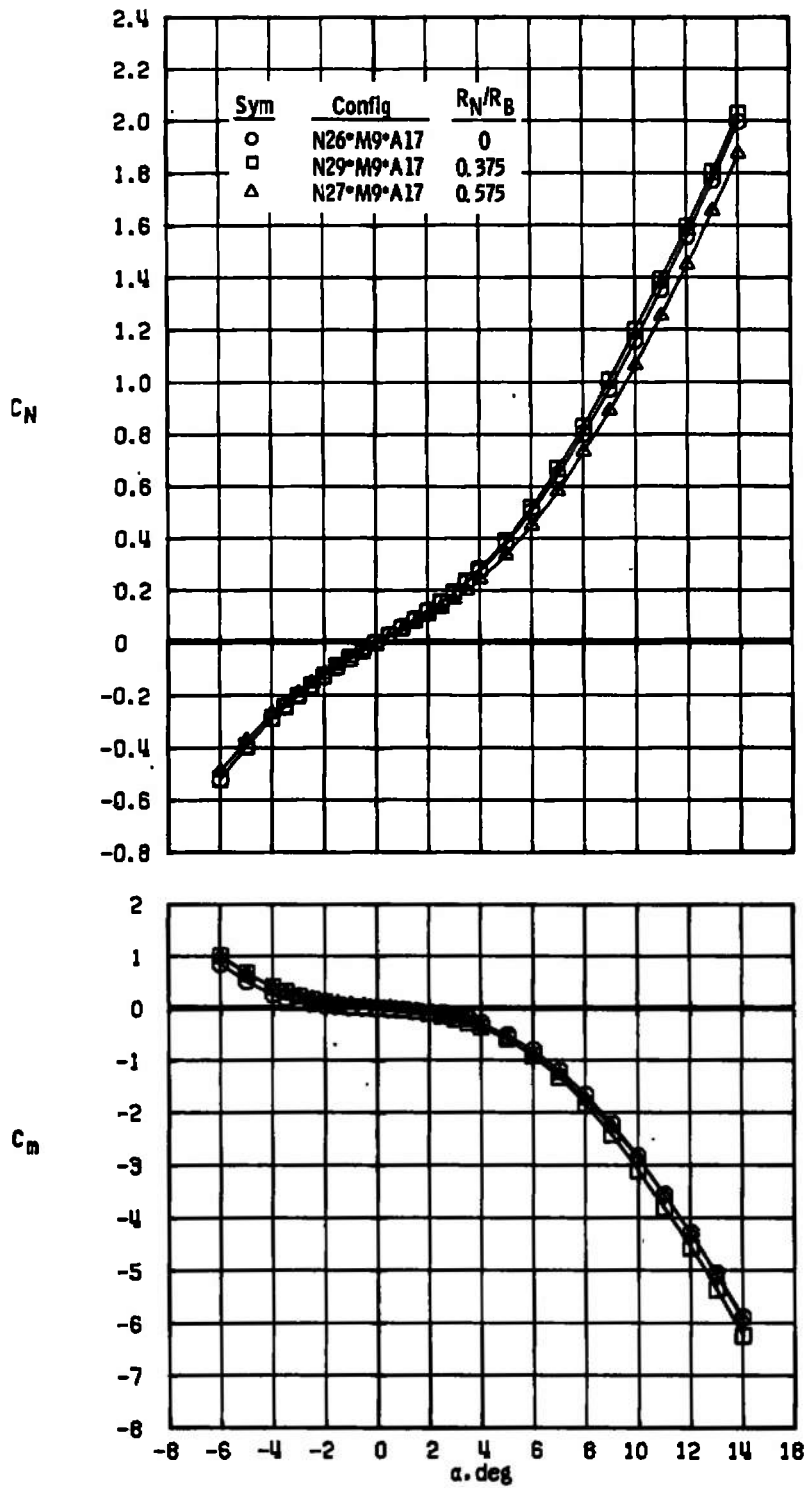


Figure 9. Effect of nose bluntness on force and moment characteristics of the 2.25-caliber nose configurations, $M_\infty = 3.01$.

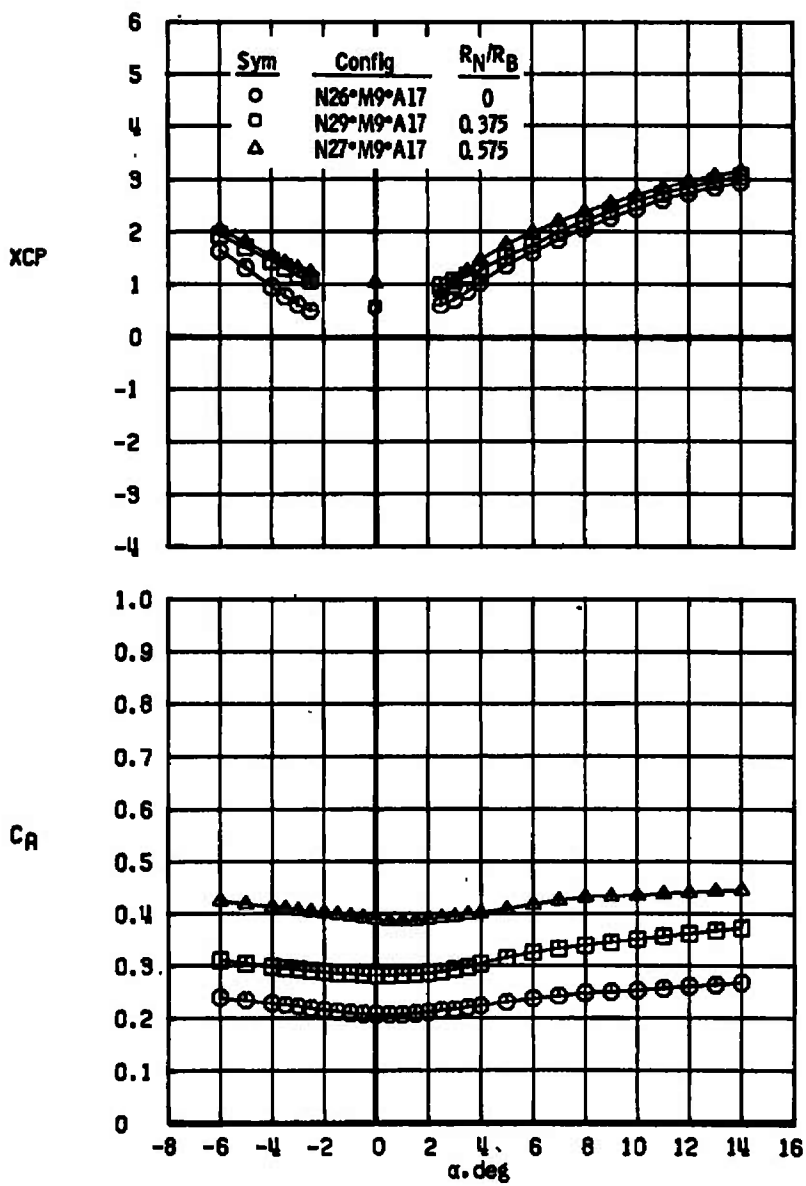


Figure 9. Concluded.

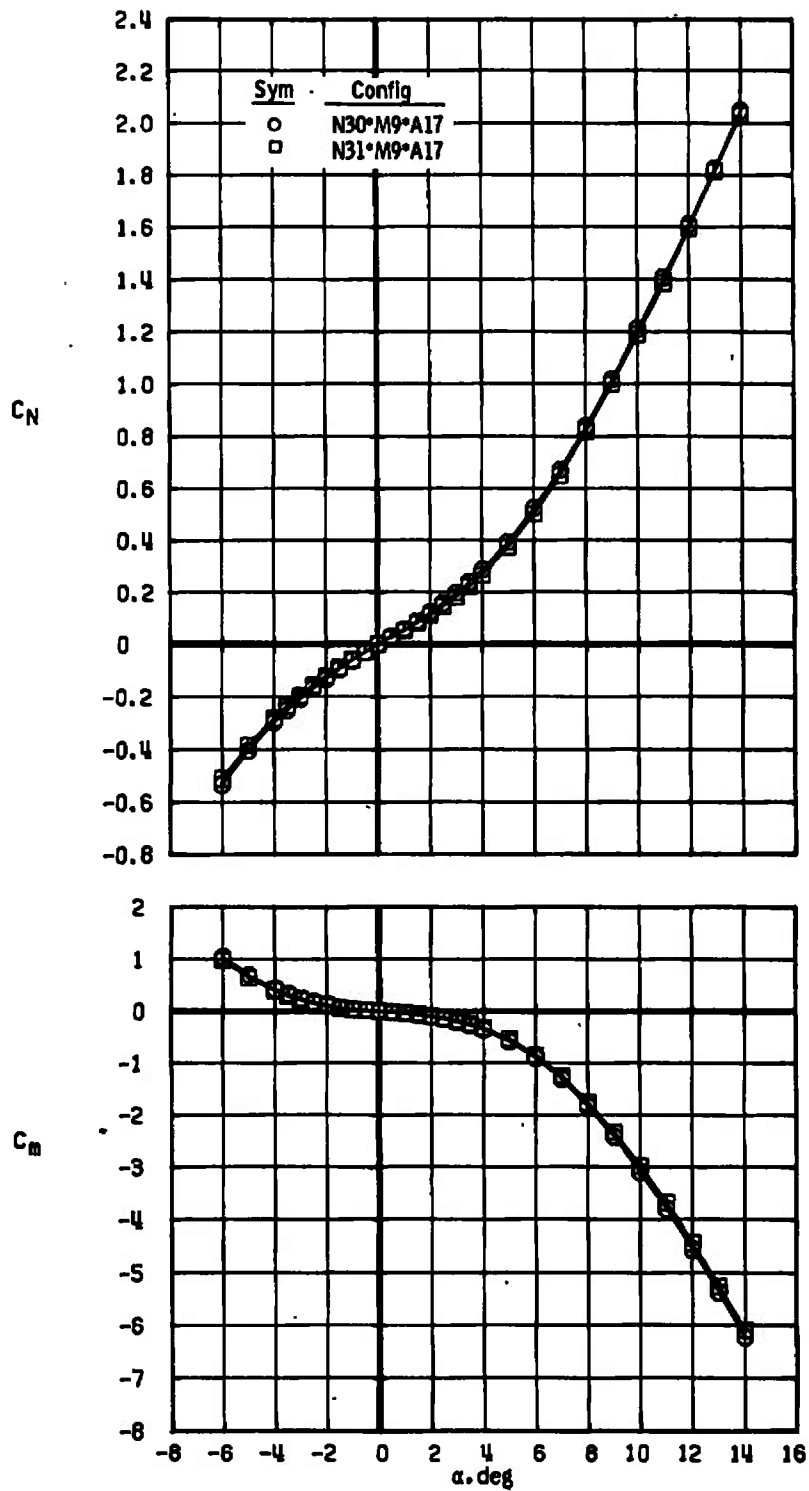


Figure 10. Power-series nose shape force and moment characteristics, $M_\infty = 3.01$.

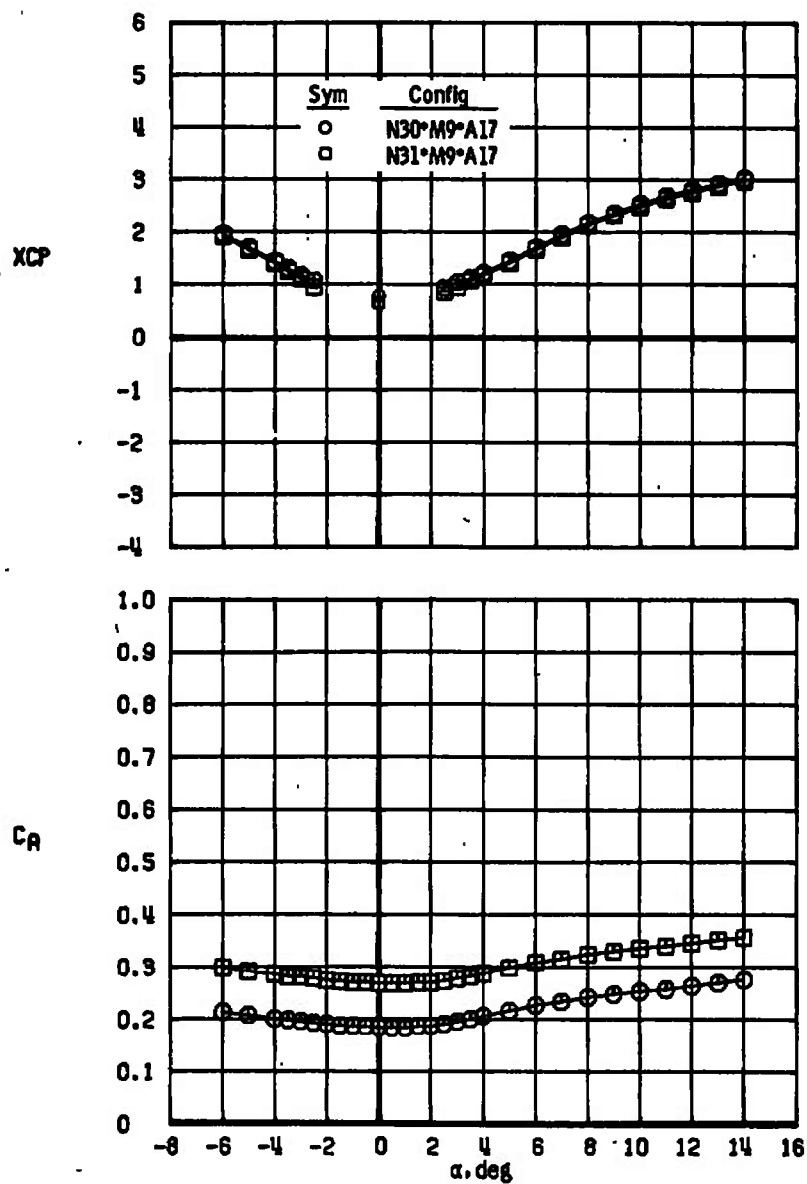


Figure 10. Concluded.

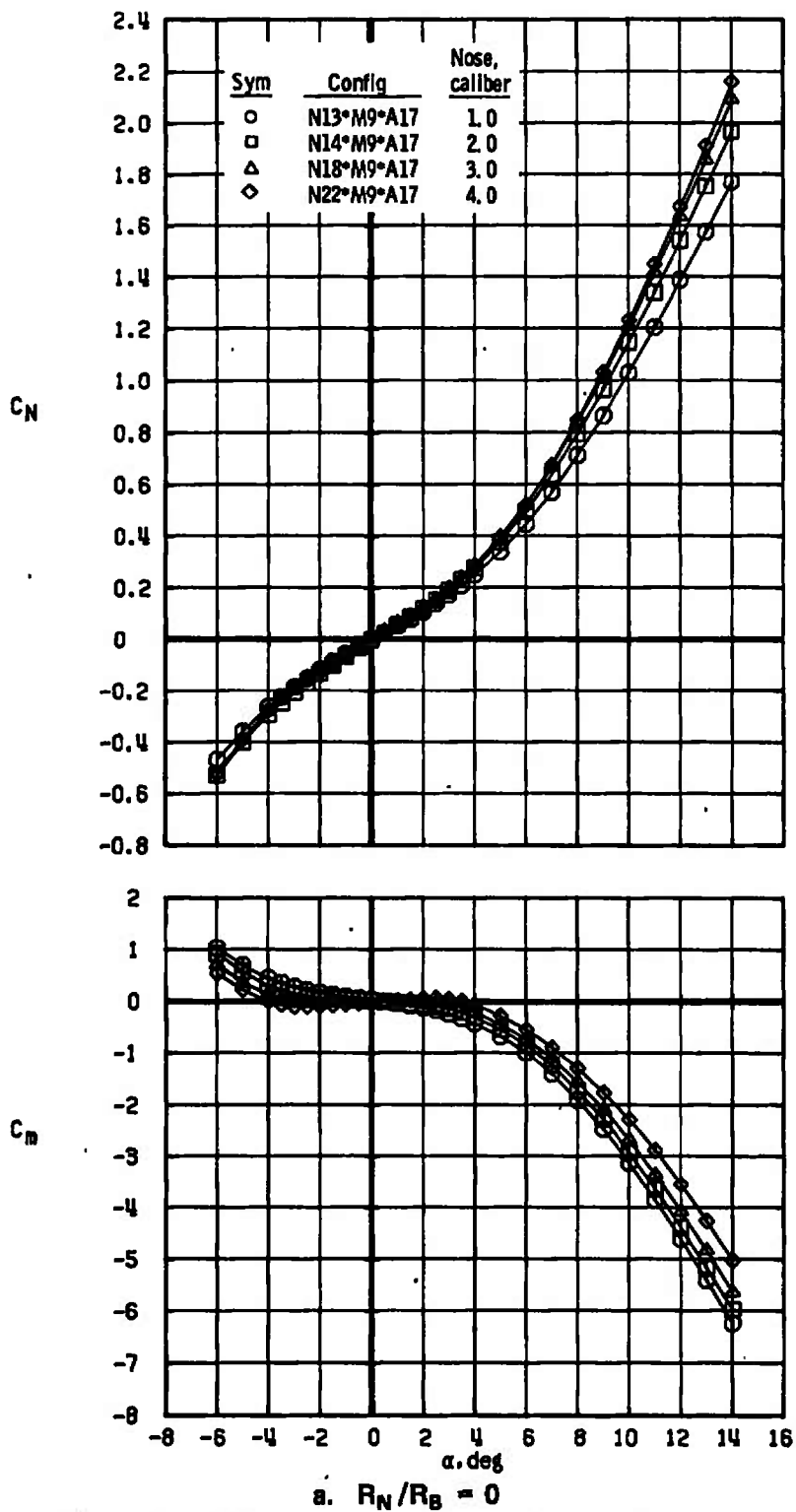
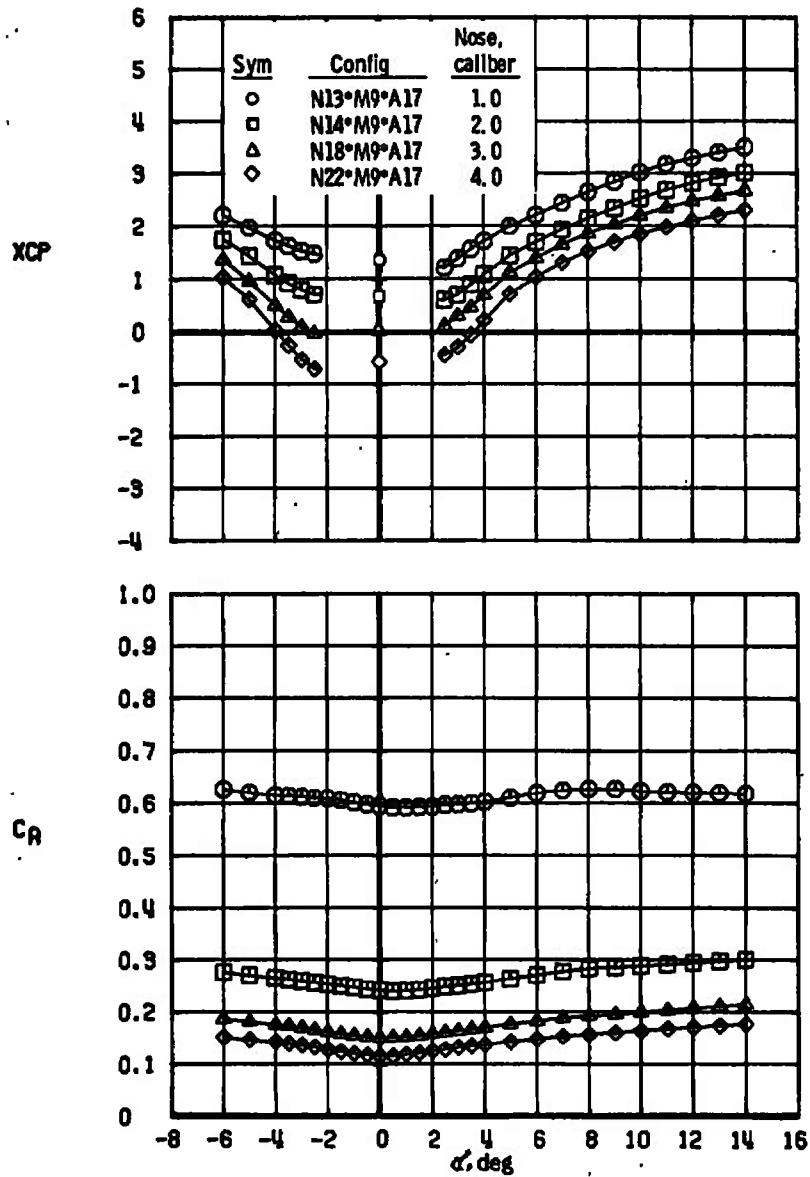
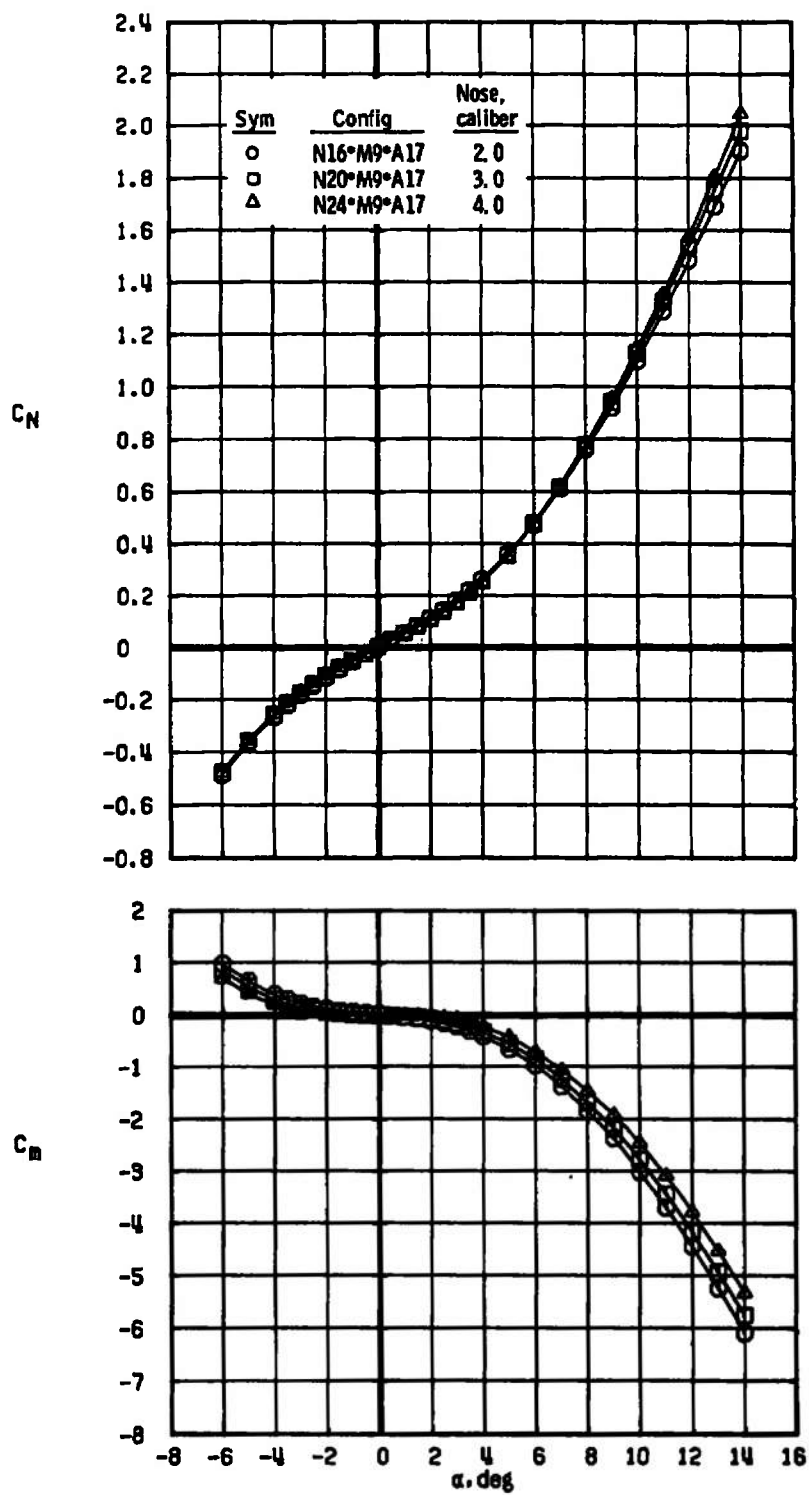


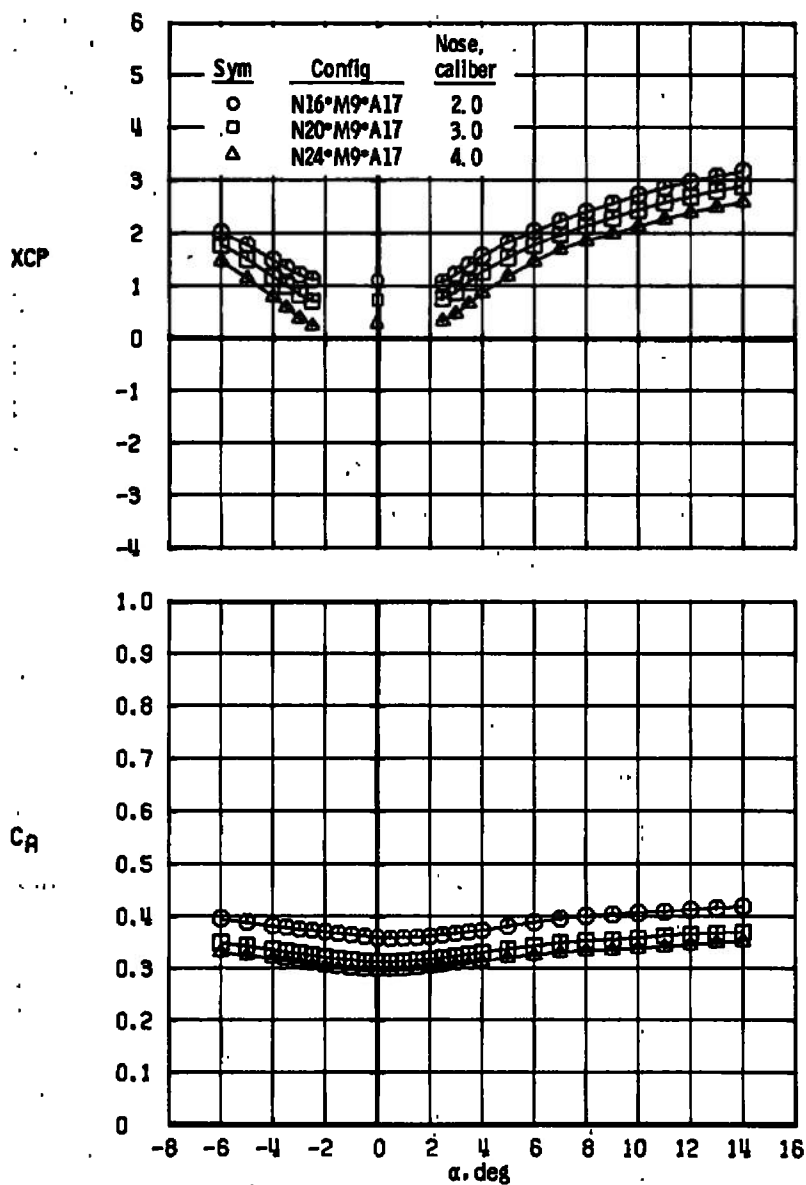
Figure 11. Effect of nose caliber on force and moment characteristics, $M_\infty = 3.01$.



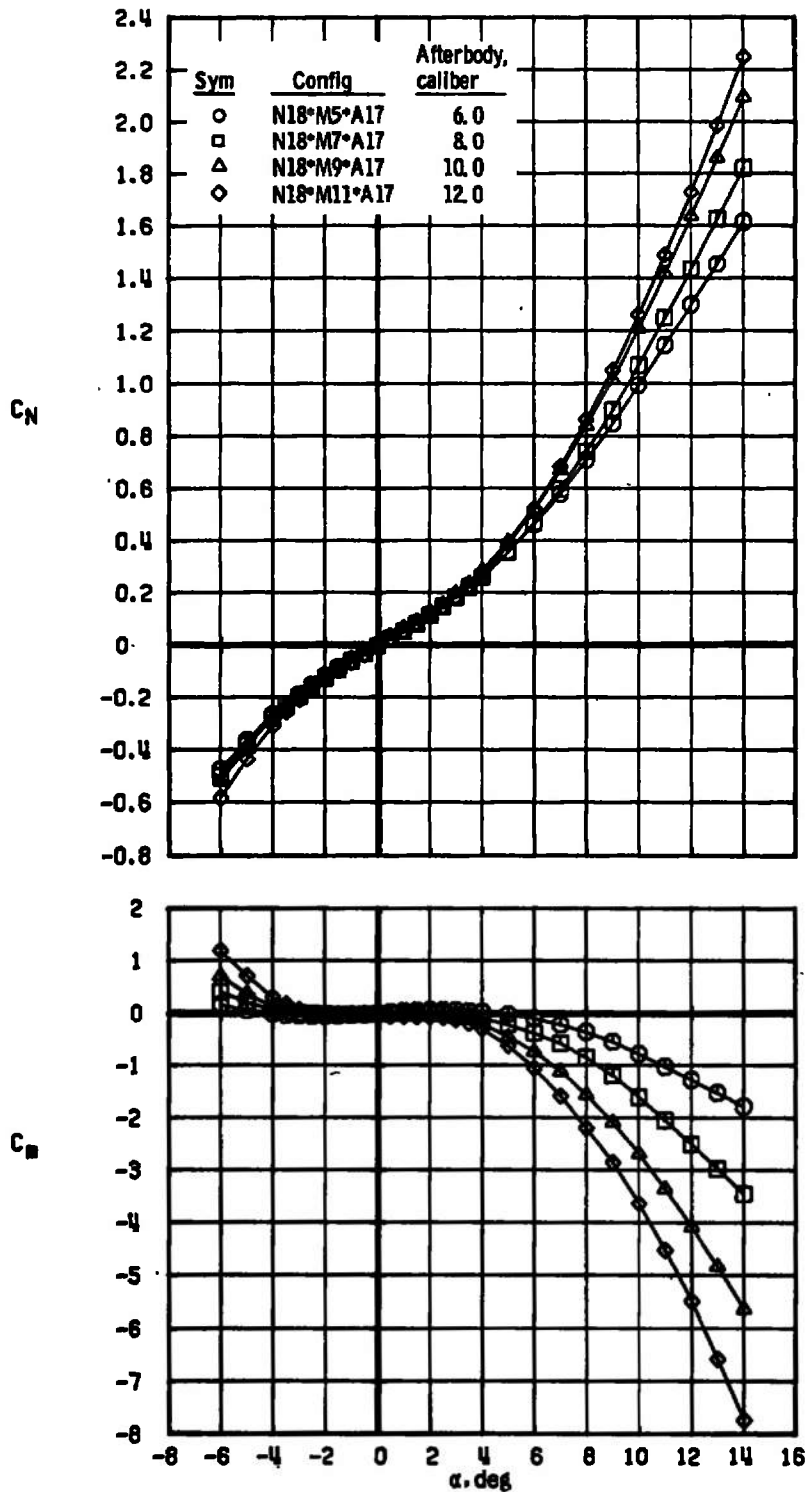
a. Concluded
Figure 11. Continued.



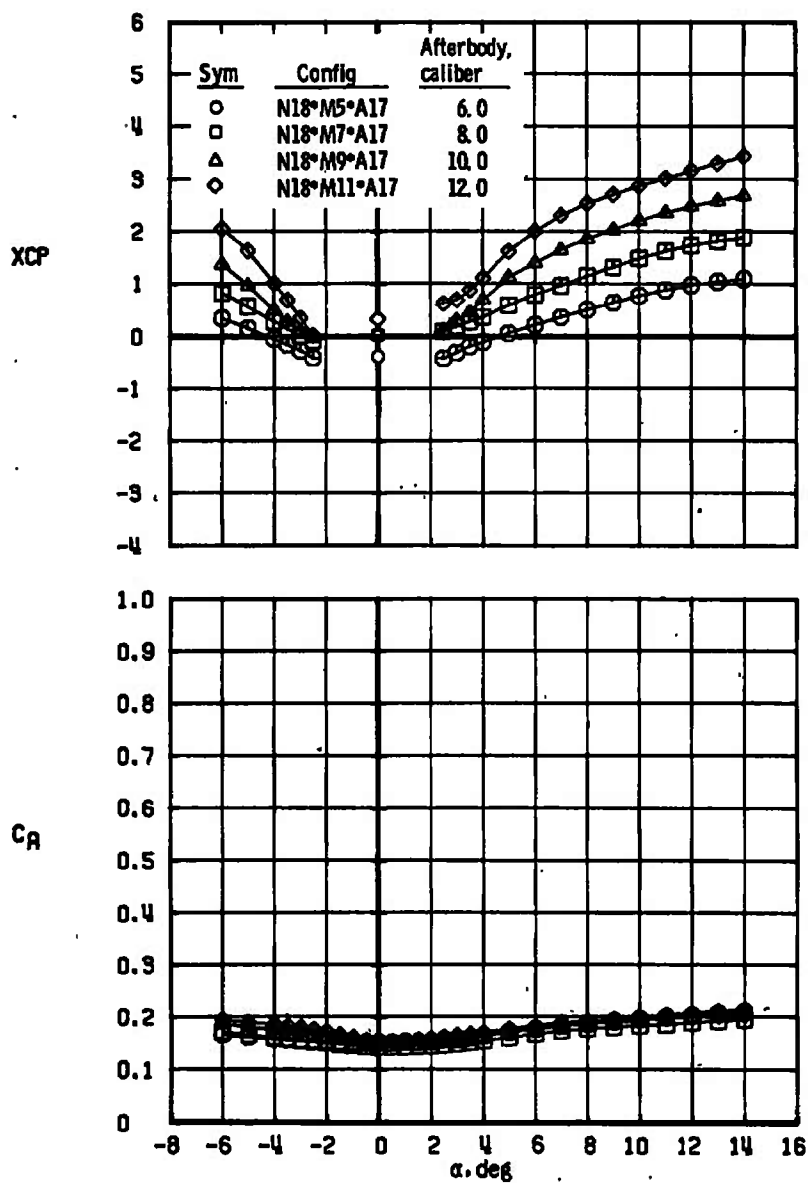
b. $R_N/R_B = 0.50$
Figure 11. Continued.



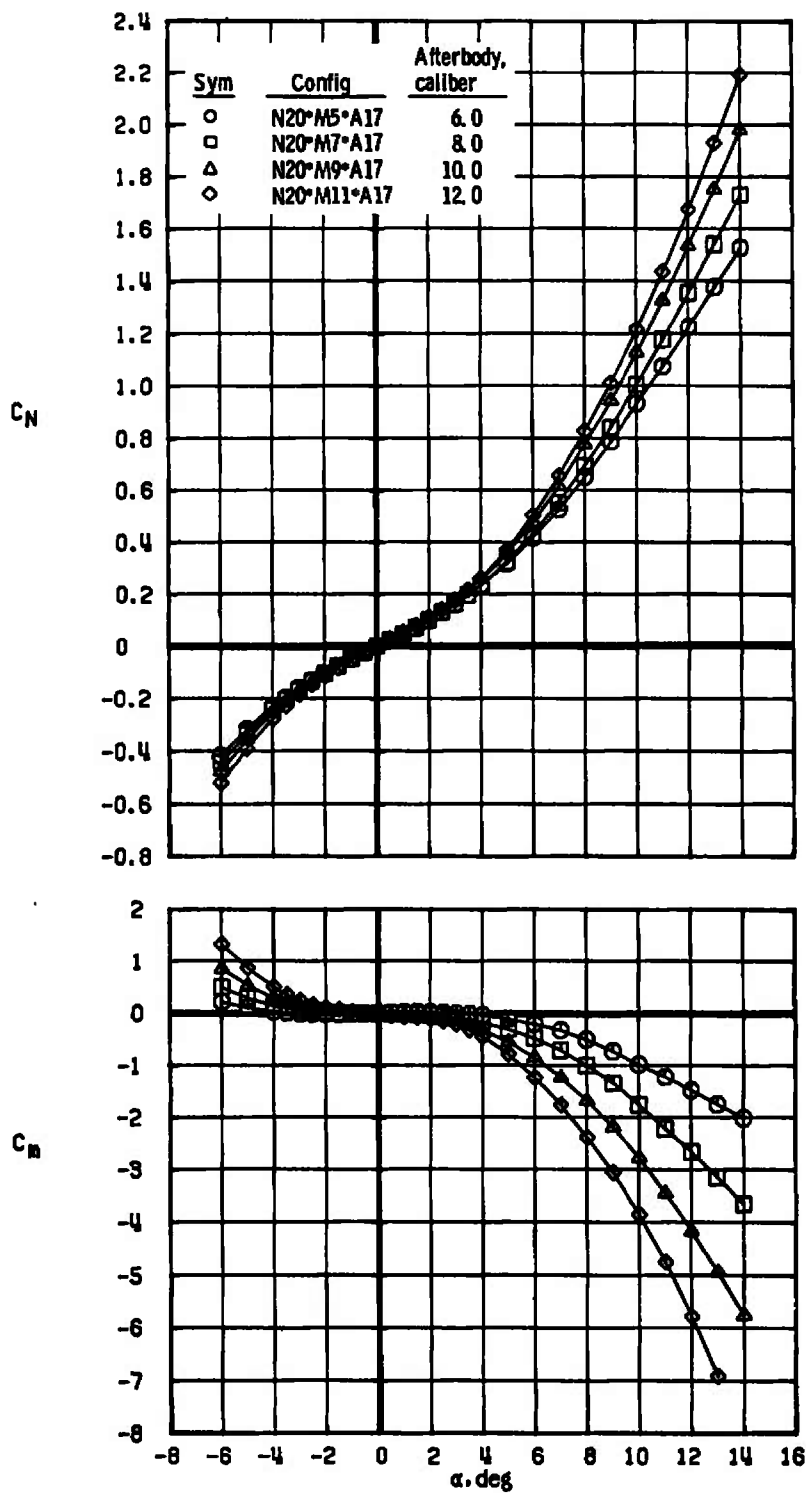
b. Concluded
Figure 11. Concluded.



a. Nose N18, $R_N/R_B = 0$
Figure 12. Effect of afterbody length on force and moment characteristics of the 3.0-caliber nose configurations, $M_\infty = 3.01$.

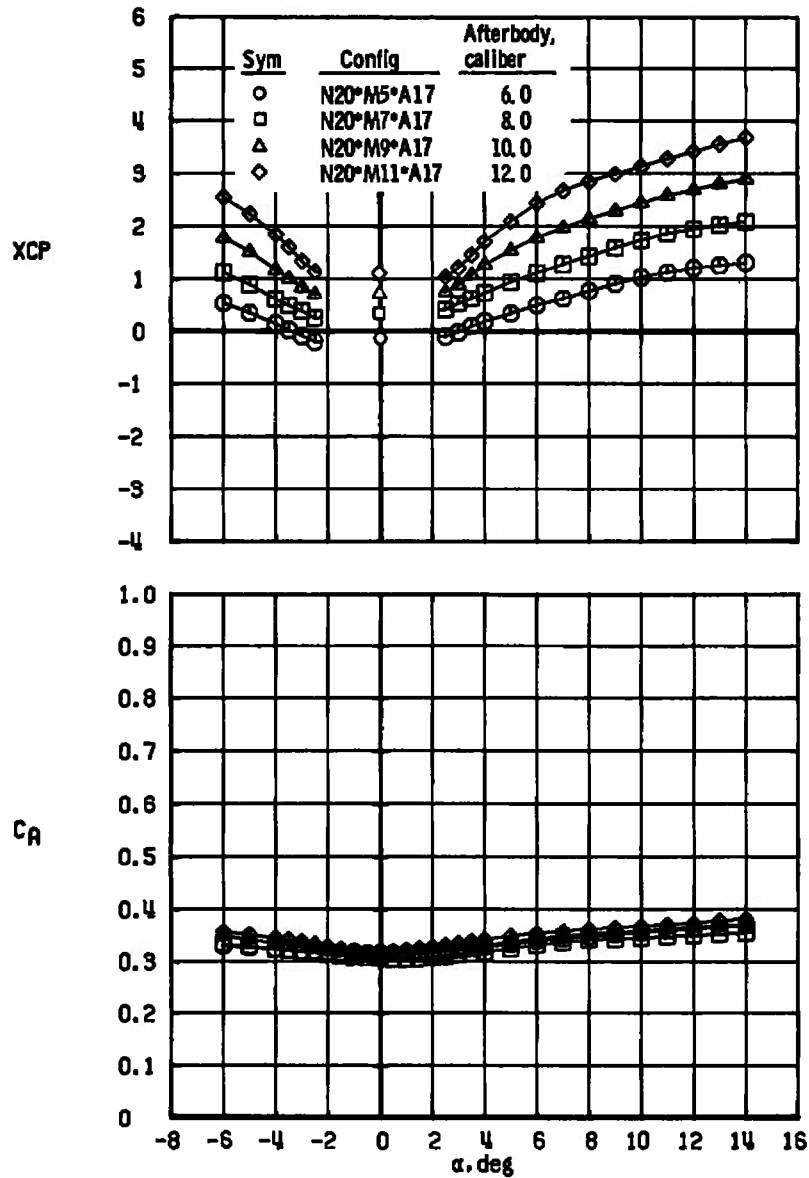


a. Concluded
Figure 12. Continued.

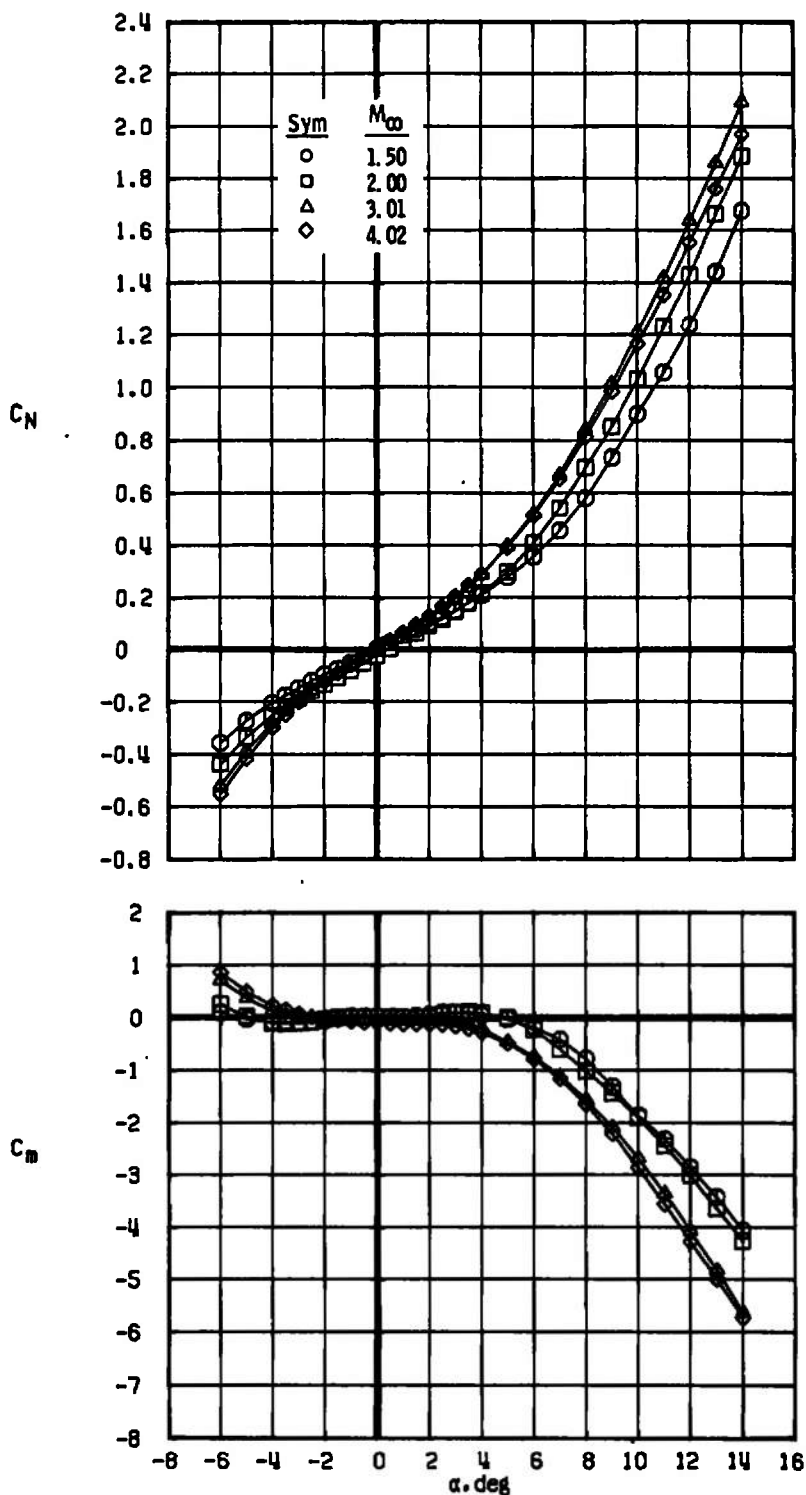


b. Nose N20, $R_N R_B = 0.50$

Figure 12. Continued.

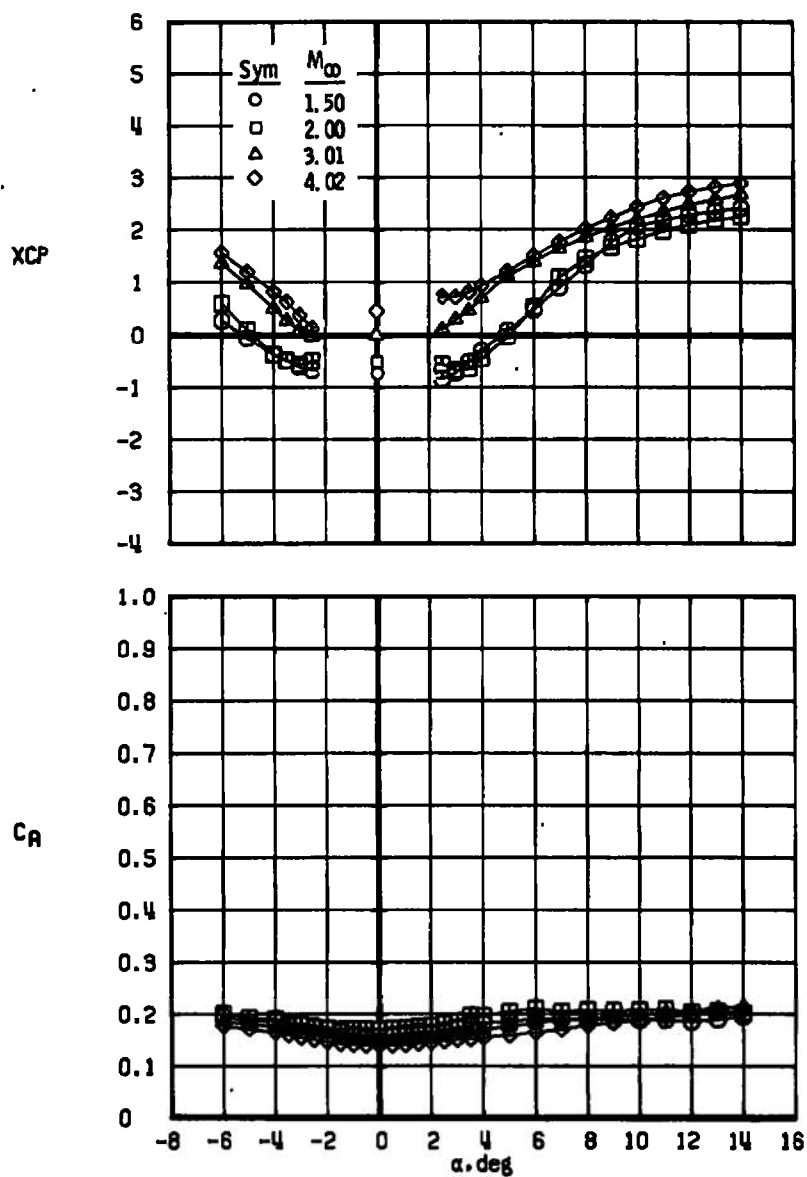


b. Concluded
Figure 12. Concluded.



a. Configuration N18*M9*A17, $R_N/R_B = 0$

Figure 13. Effect of Mach number on force and moment characteristics of the 3.0-caliber nose configurations.



a. Concluded
Figure 13. Continued.

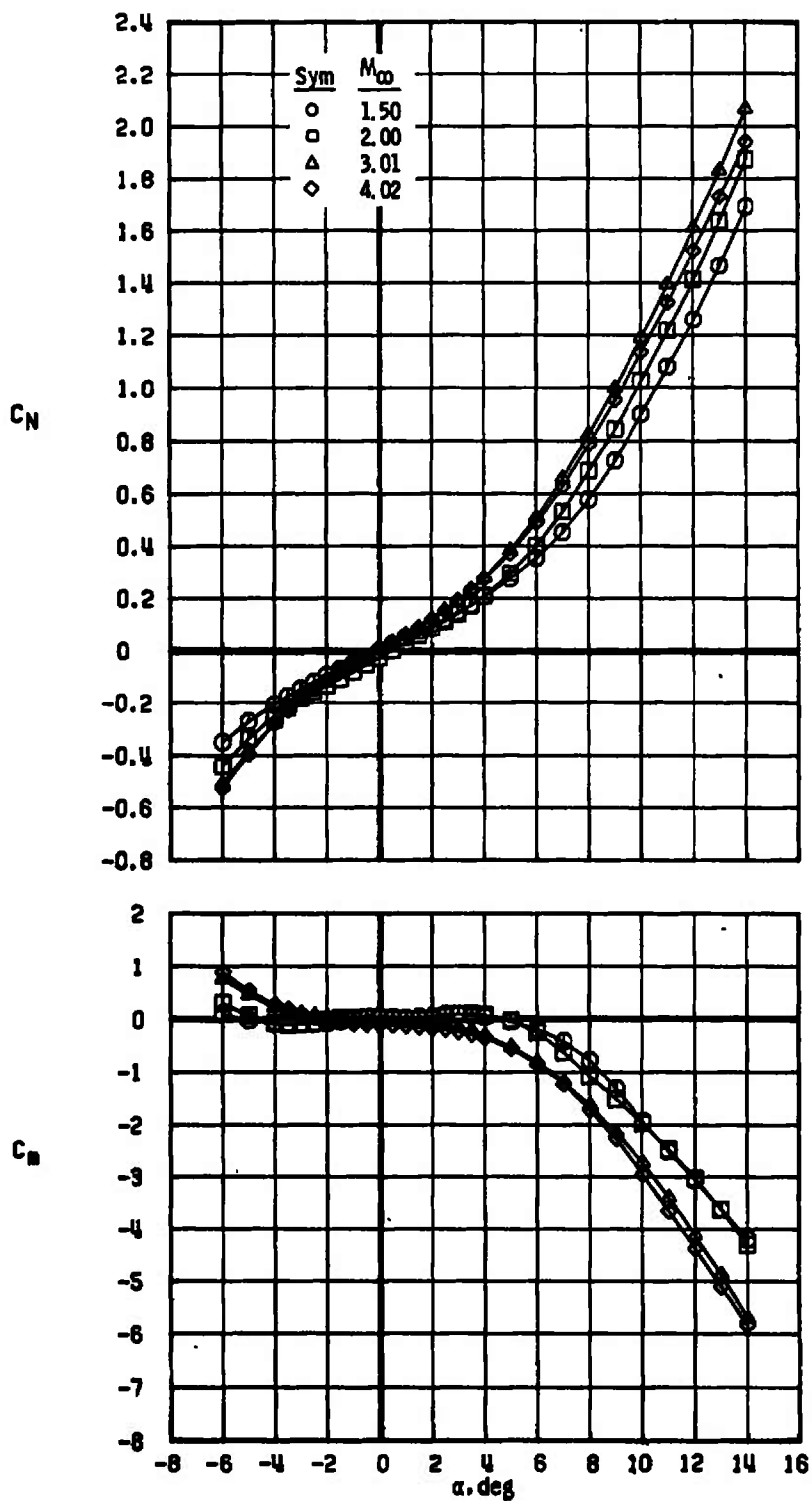
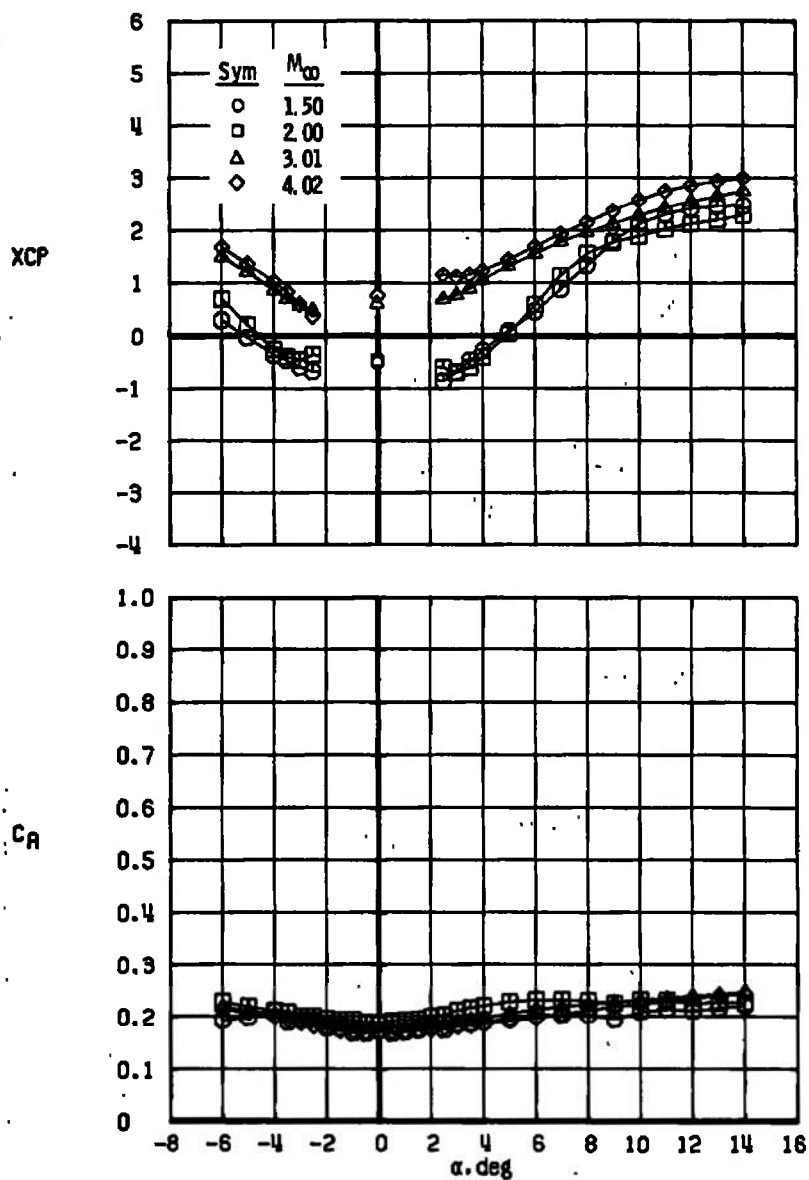
b. Configuration N19*M9*A17, $R_N/R_B = 0.25$

Figure 13. Continued.



b. Concluded
Figure 13. Continued.

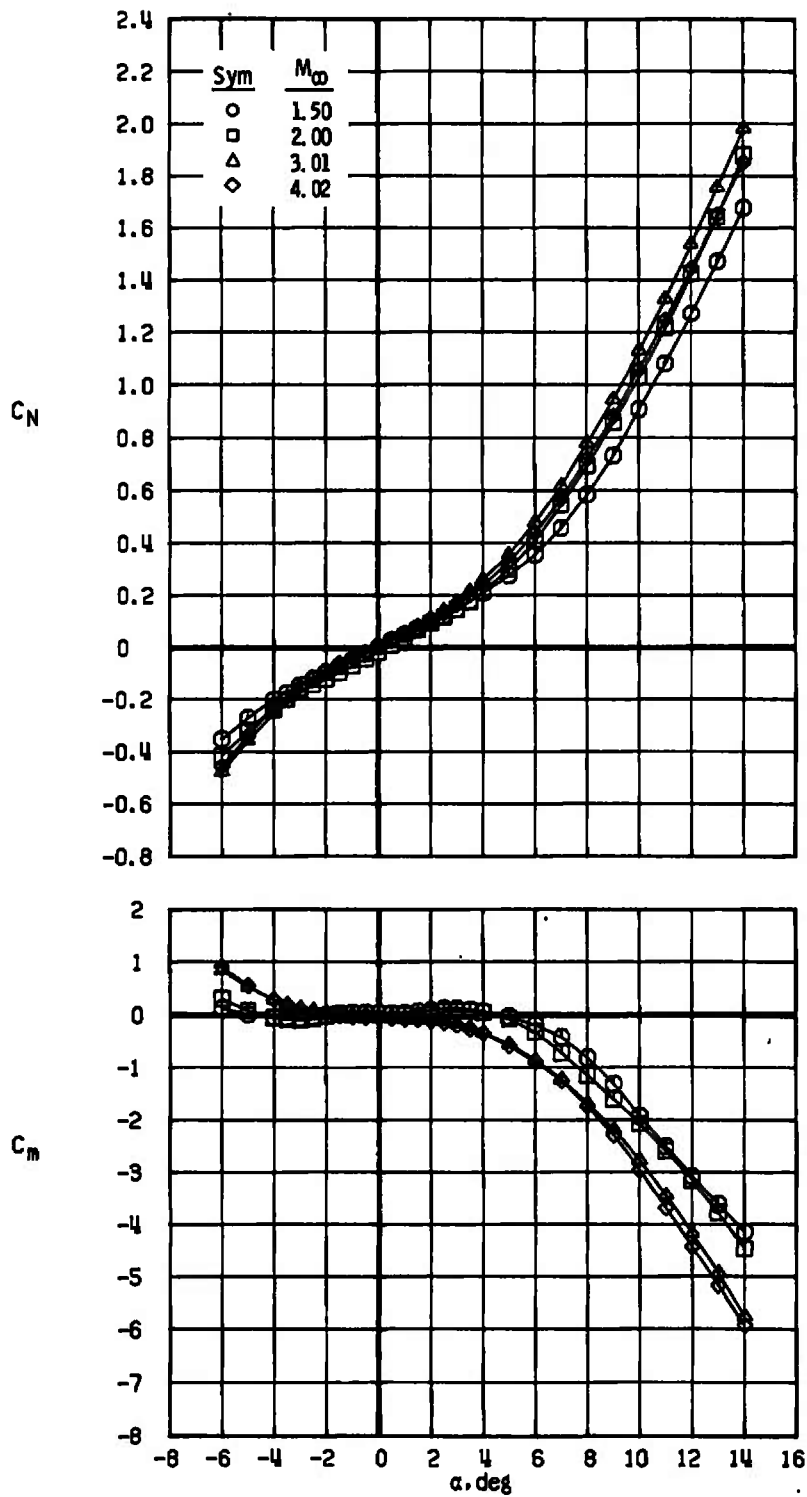
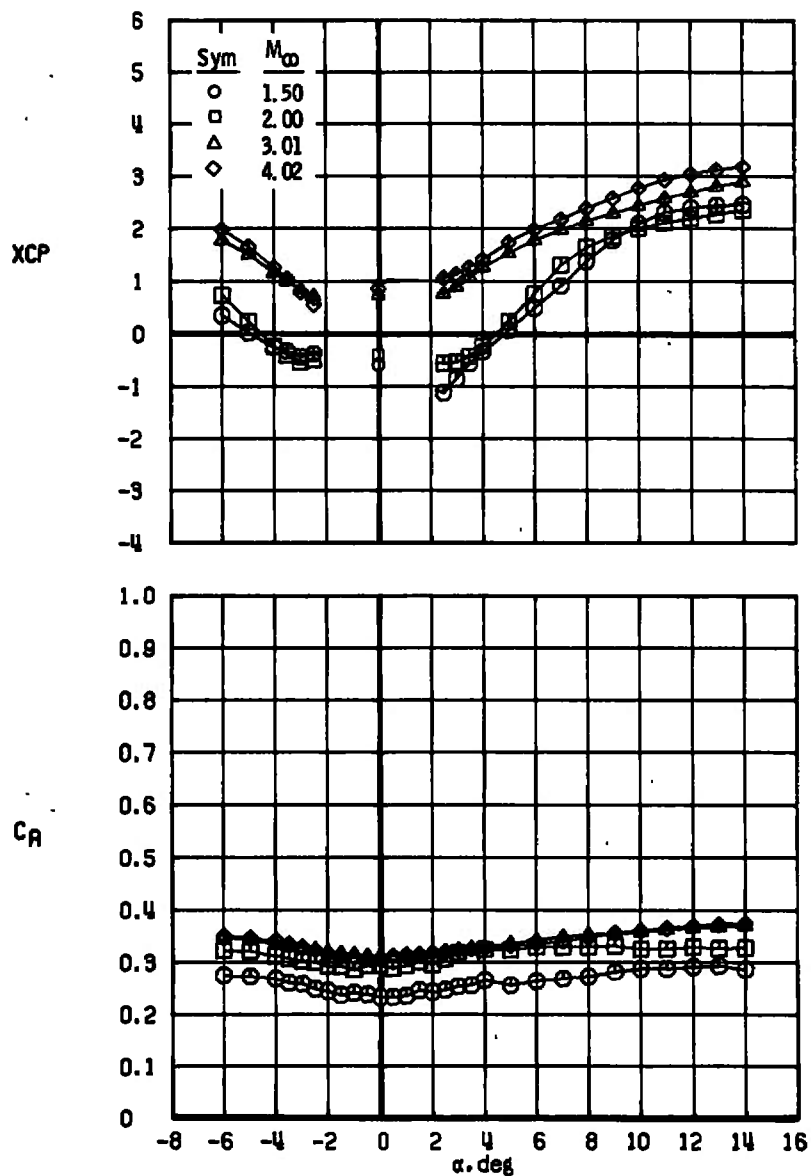
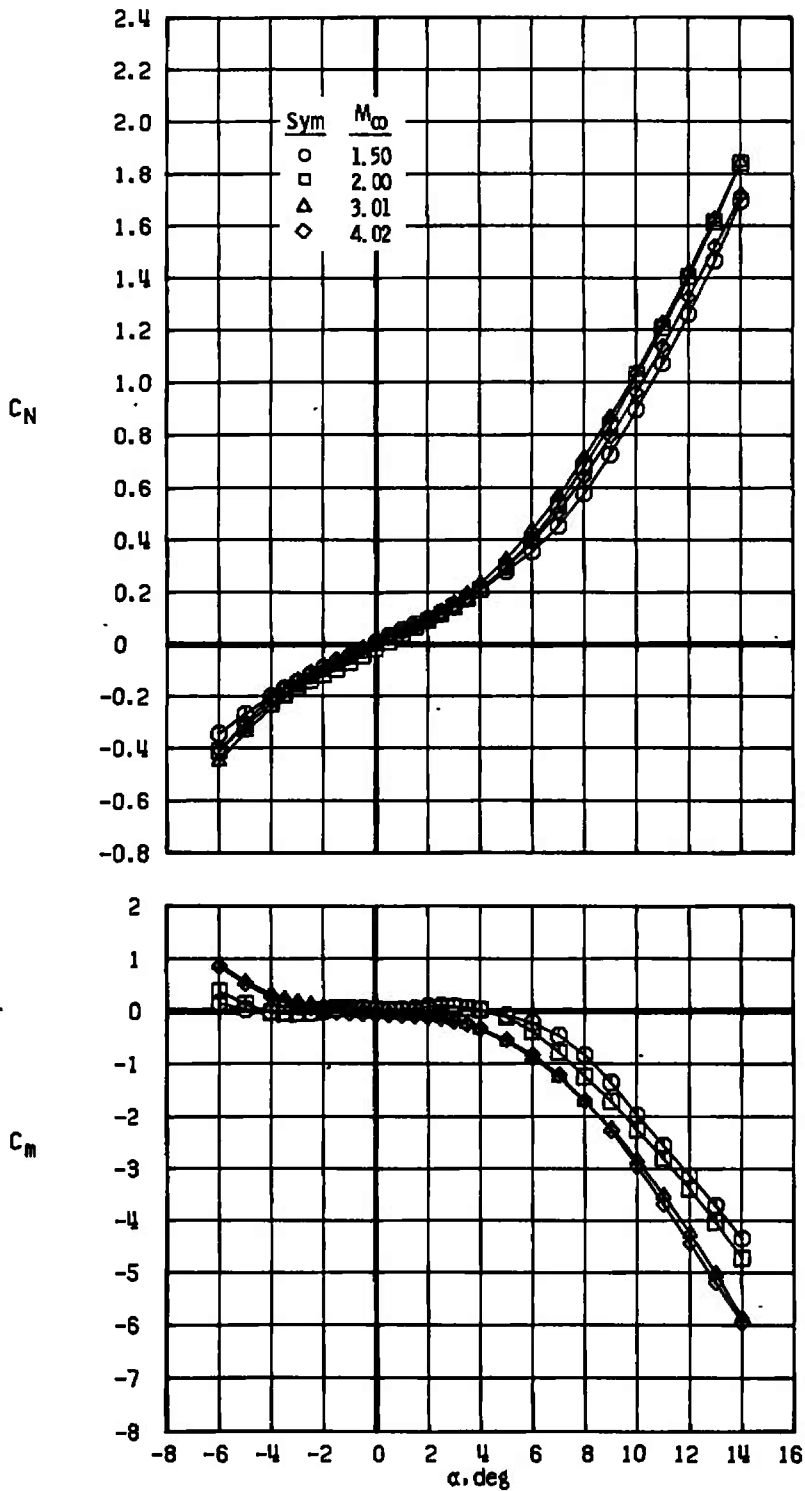
c. Configuration N20*M9*A17, $R_N/R_B = 0.50$

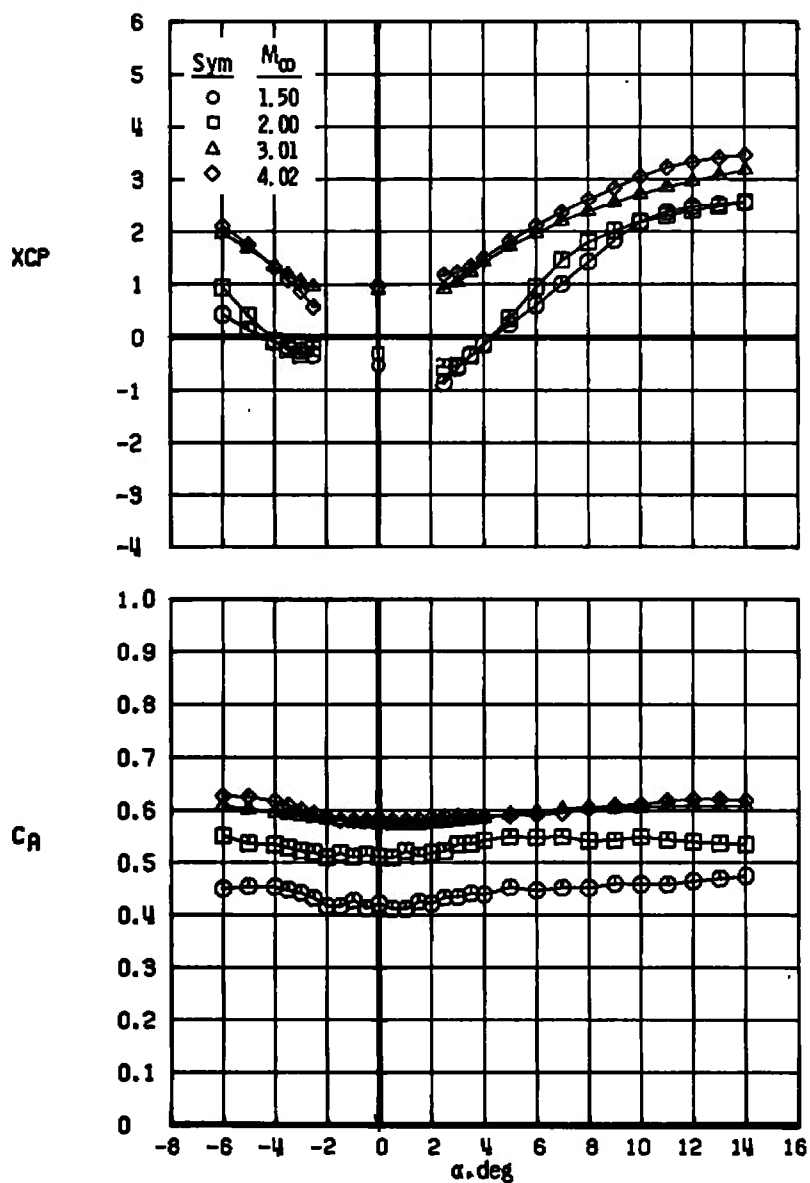
Figure 13. Continued.



c. Concluded
Figure 13. Continued.



d. Configuration N21*M9*A17, $R_N/R_B = 0.75$
Figure 13. Continued.



d. Concluded
Figure 13. Concluded.

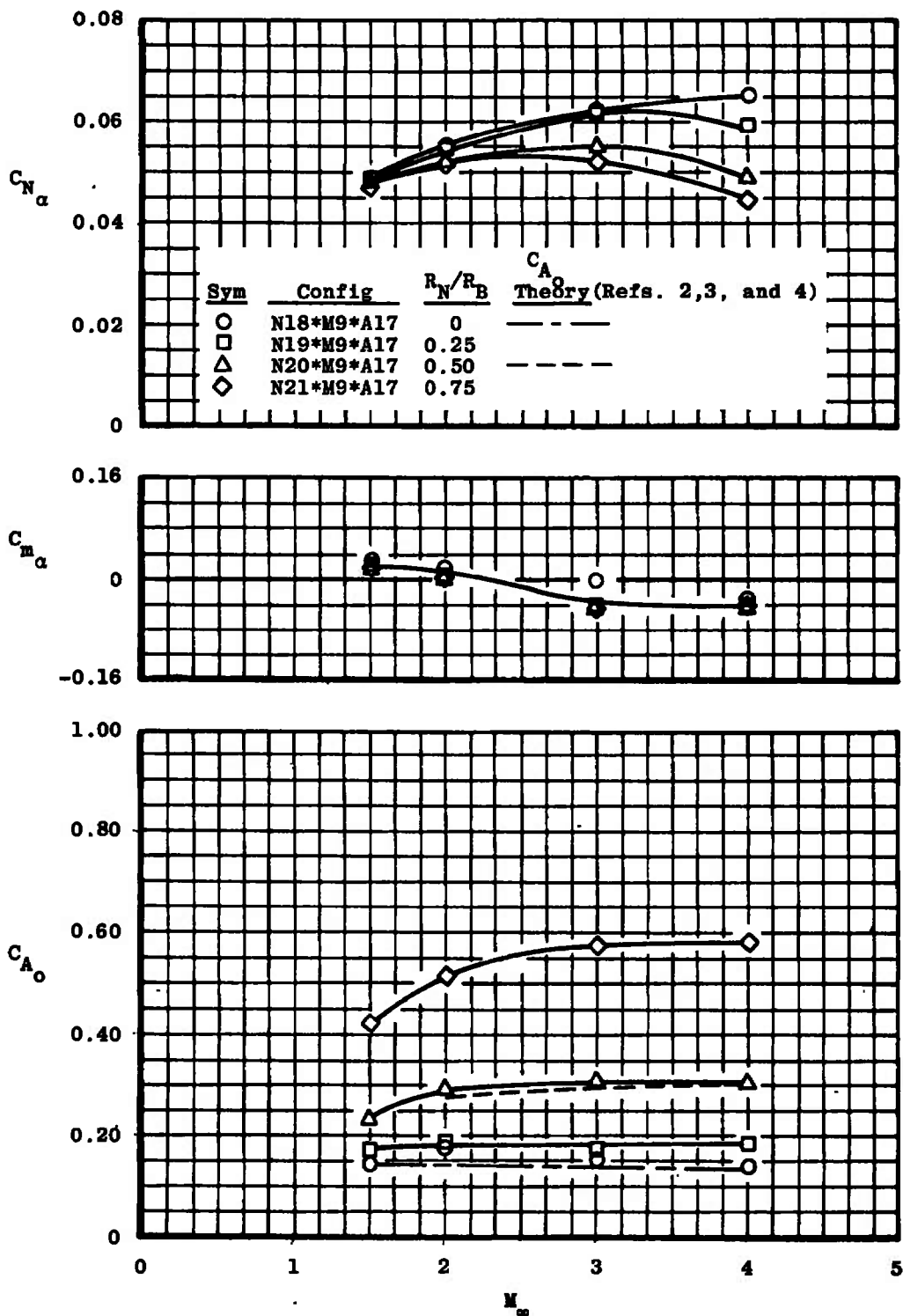
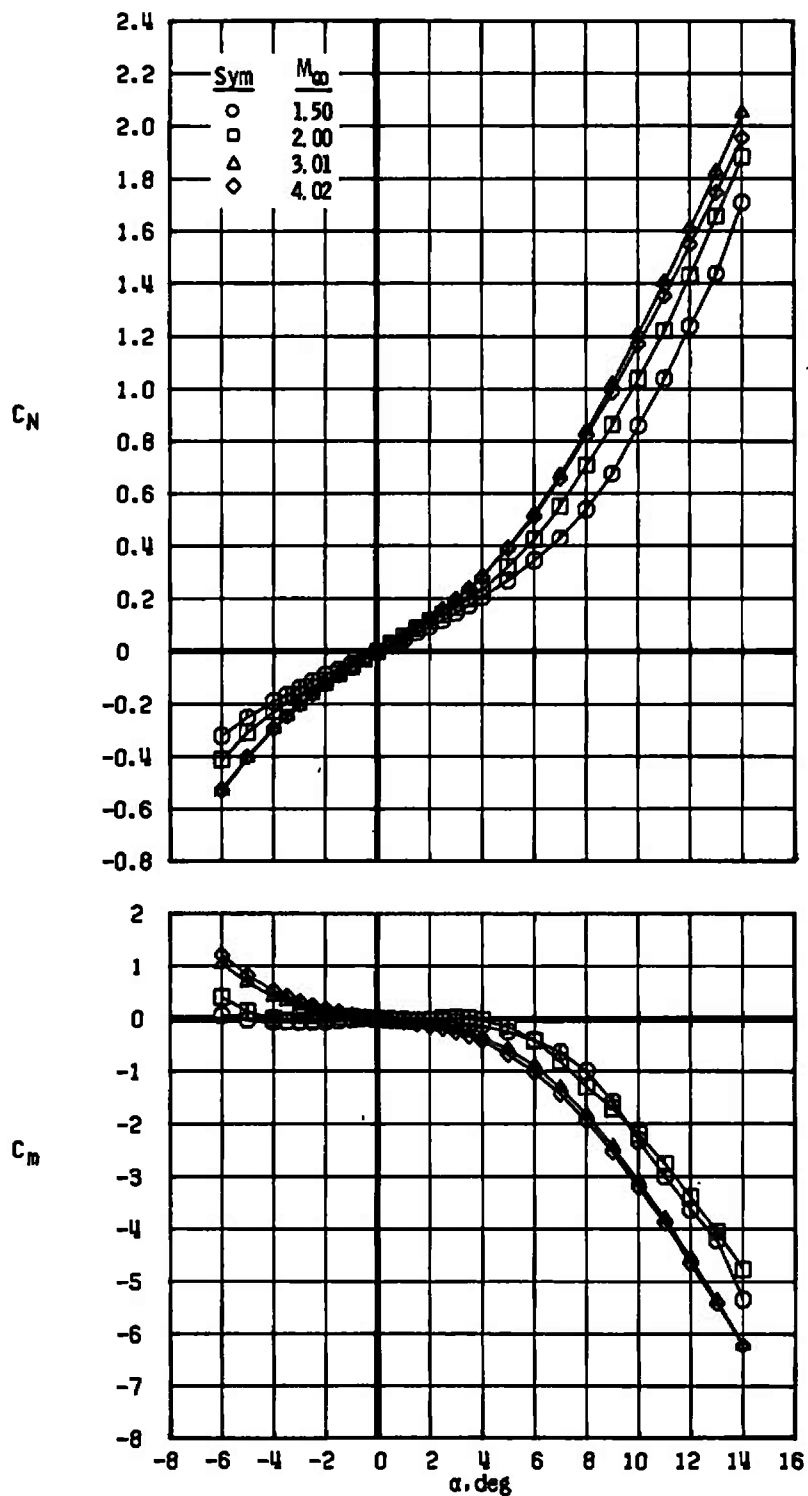
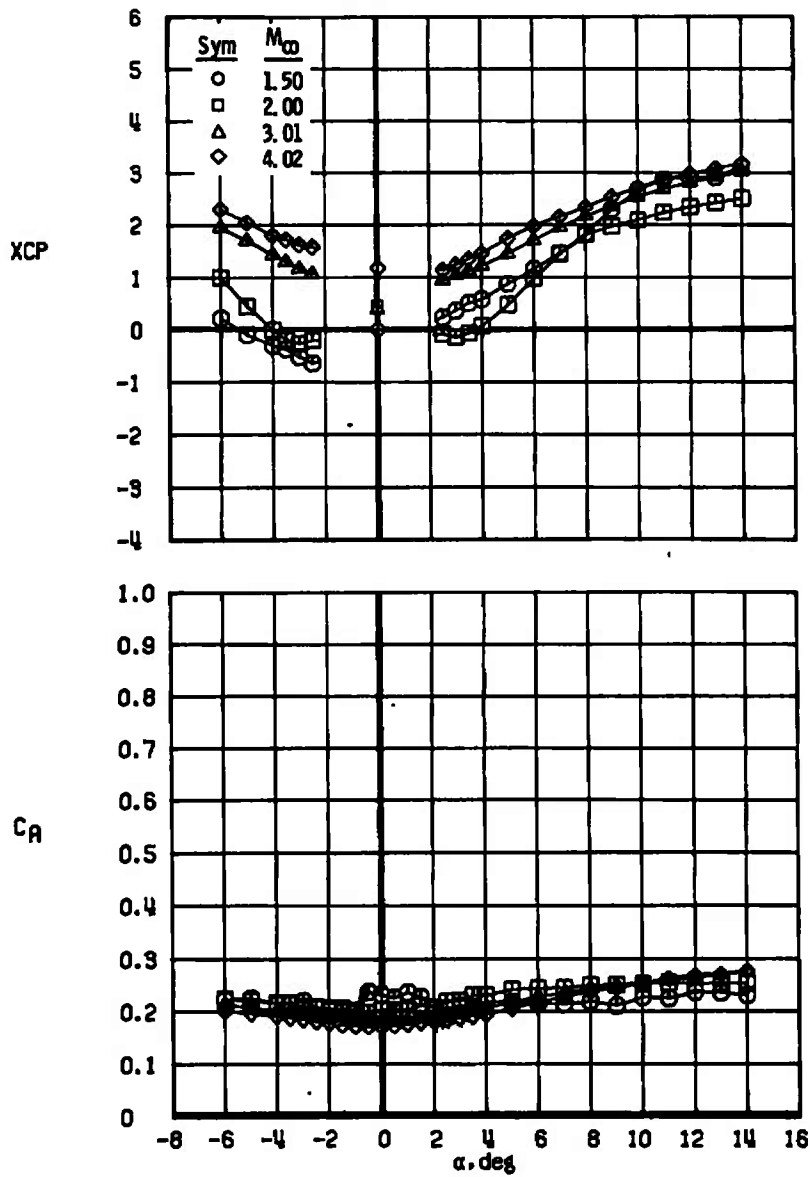


Figure 14. Variation of C_{N_α} , C_{m_α} , and C_{A_0} with Mach number and comparisons with theoretical C_{A_0} for 3.0-caliber nose configurations.

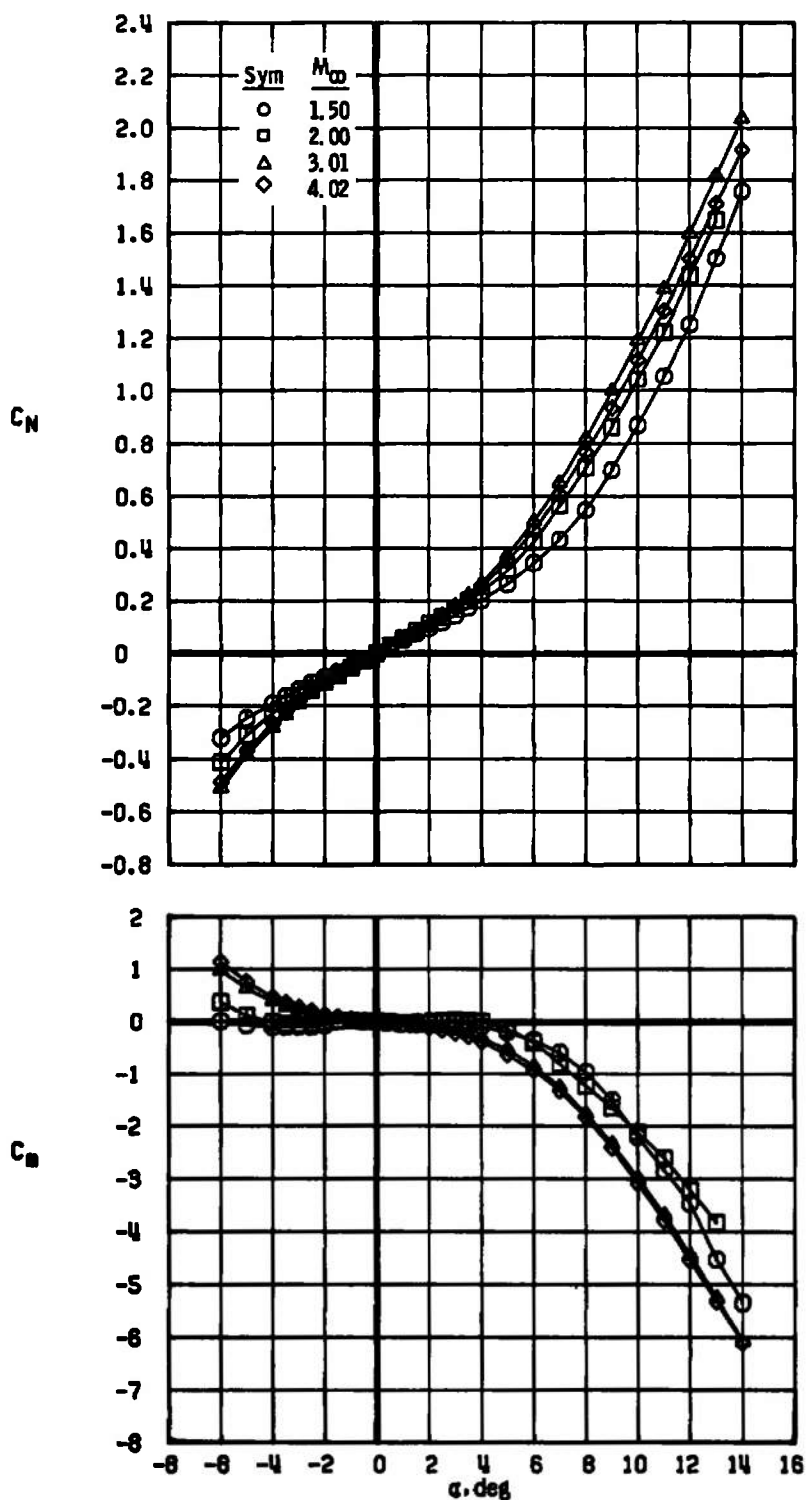


a. Configuration N30*M9*A17

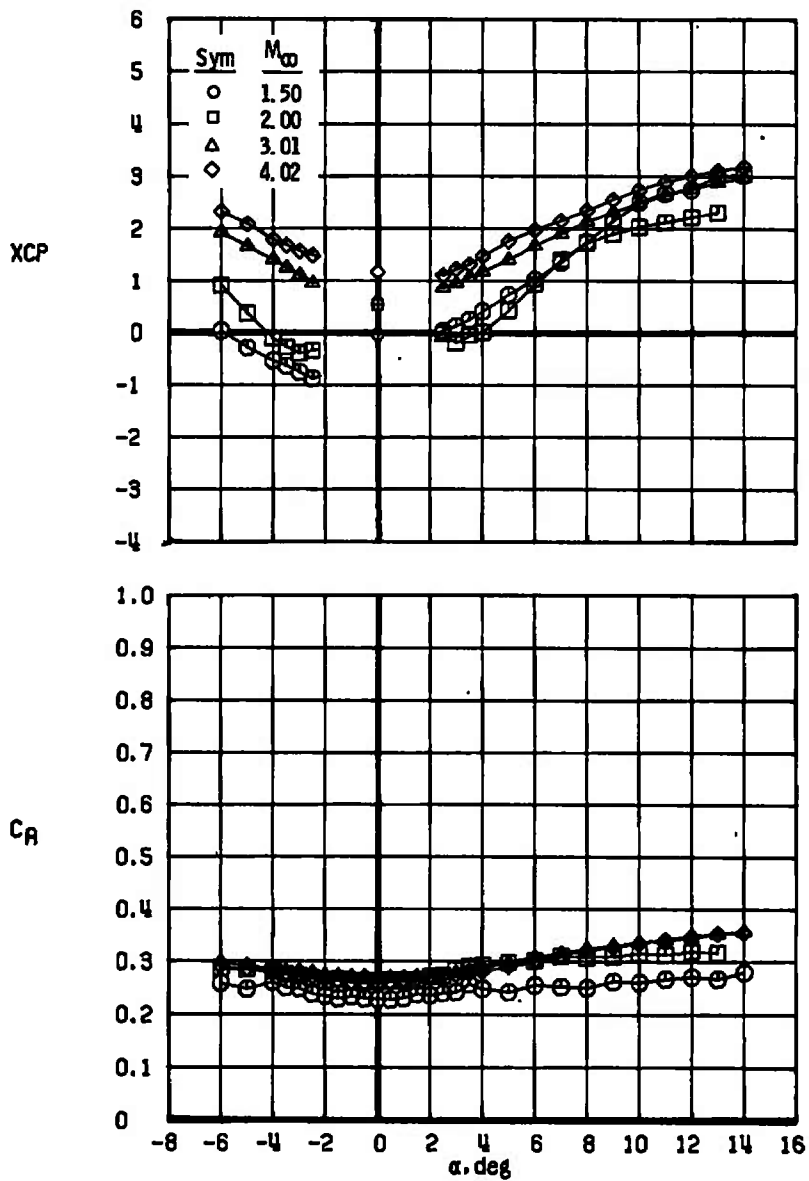
Figure 15. Effect of Mach number on force and moment characteristics of the power-series nose configurations.



a. Concluded
Figure 15. Continued.



b. Configuration N31*M9*A17
Figure 15. Continued.



b. Concluded
Figure 15. Concluded.

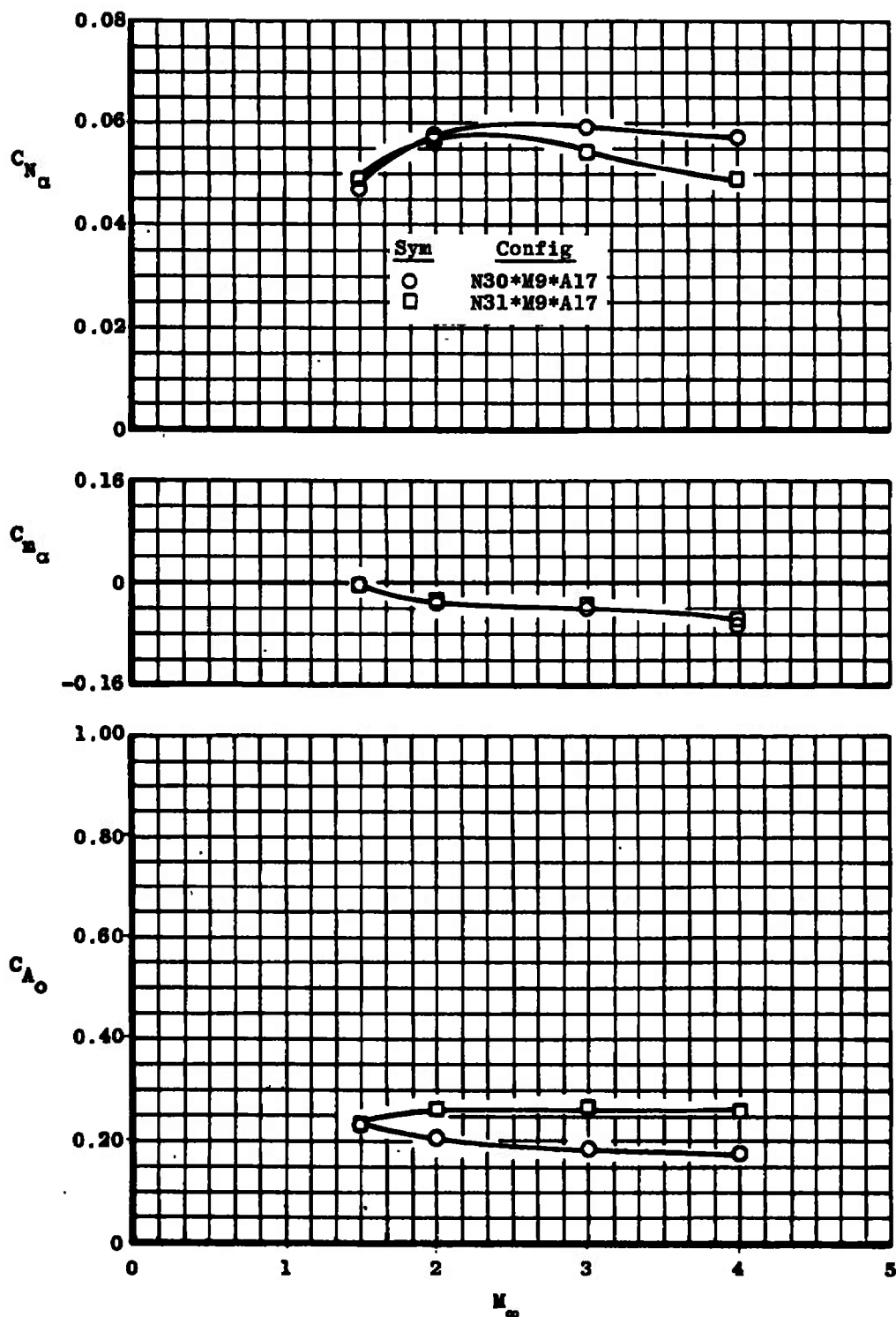


Figure 16. Variation of C_{N_α} , C_{m_α} , and C_{A_0} with Mach number for the power-series nose configurations.

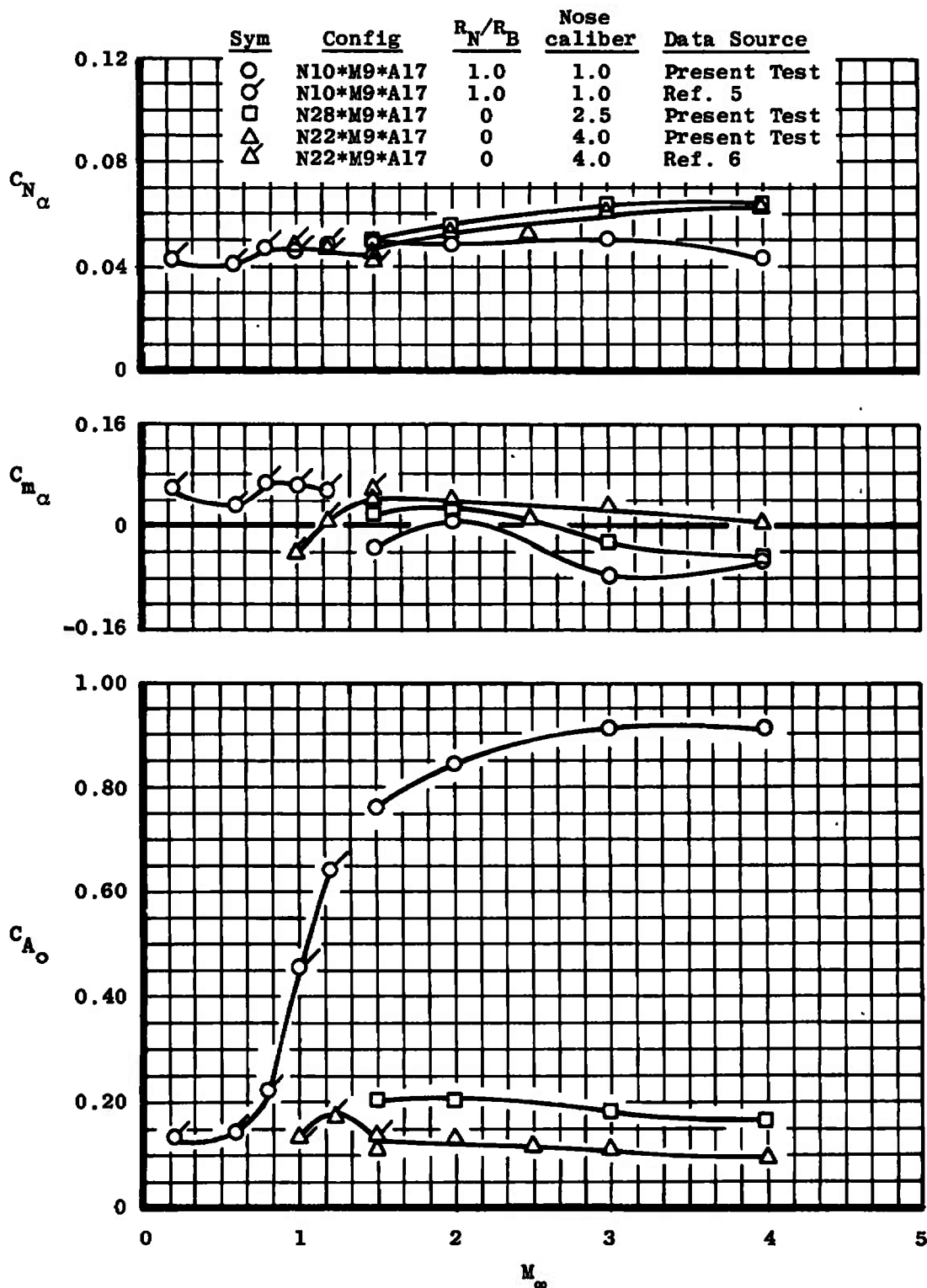


Figure 17. Variation of $C_{N\alpha}$, $C_{m\alpha}$, and C_{Ao} with Mach number and comparisons with subsonic and transonic results from other test programs.

Table 1. Test Summary

Config	α^1 Schedule	ϕ^1 Schedule	Mach Number						
			1.5	2.0	2.5	3.0	3.5	4.0	4.5
<u>N10*M5*A17</u>	A	0	x						
↓	B	0	x	x		x			
	B	180	x						
	C	0	x						
	C	180	x						
	B	0	x	x		x			
N13			x	x		x			
N14			x	x		x			
N15			x	x		x			
N16			x	x		x			
N17			x	x		x			
N18			x	x		x*			
N19			x	x		x			
N20			x	x		x*			
N21			x	x		x			
N22			x						
↓	A	0	x						
	B	0	x	x ²		x ²			
	B	180	x						
	C	0	x						
	C	180	x						
	B	0	x	x		x			
N23			x	x		x			
N24			x	x		x			
N25			x	x		x			
N26			x	x	x	x	x	x	x
↓	A	0	x	x	x	x	x	x	x
	B	90		x					
	B	-90		x					
	C	0	x	x		x	x	x	x
N27			x	x		x	x	x	x
N27			x	x	x	x	x	x	x
N27			x	x		x	x	x	x
N28			x	x		x			
N29			x	x		x			
N30			x	x		x			
N31			x	x		x			
<u>N10*M7*17</u>	B	0	x	x		x		x	
N13			x	x		x		x	
N14			x	x		x		x	
N15			x	x		x		x	
N16			x	x		x		x	
N17			x	x		x		x	
N18			x	x		x*		x	
N19			x	x		x		x	
N20			x	x		x*			
N21			x	x		x		x	
N22			x	x		x		x	
N23			x	x		x		x	
N24			x	x		x			
N25			x	x		x		x	
N28			x	x		x			

Table 1. Concluded

Config	α Schedule	ϕ Schedule	Mach Number						
			1.5	2.0	2.5	3.0	3.5	4.0	4.5
N10*M9*A17	B	0	x*	x*		x*		x*	
N13			x	x		x*		x	
N14			x	x		x*		x	
N15			x	x		x		x	
N16			x	x		x*		x	
N17			x	x		x		x	
N18			x*	x*		x*		x*	
N19			x*	x*		x*		x*	
N20			x*	x*		x*		x*	
N21			x*	x*		x*		x*	
N22			x	x	x	x*		x	
N23			x	x		x		x	
N24			x	x		x*		x	
N25			x	x		x		x	
N26			x	x	x	x*		x	
N26	C	0	x						
N26	0	0				x			
N27	B	0	x	x	x	x*		x	
N27	C	0	x						
N28	B	0	x	x		x		x	
N29	A	0		x					
N29	B	0	x	x		x*		x	
N30			x*	x*		x*		x*	
N31			x*	x*		x*		x*	
N10*M11*A17	A	0	x						
	B	0	x	x		x		x	
	C	180	x	x					
	B	0	x						
N13				x		x			
N14			x	x		x			
N15			x	x		x			
N16			x	x		x			
N17			x	x		x			
N18			x	x		x*			
N19			x	x		x			
N20			x	x		x*			
N21			x	x		x			
N22			x	x		x			
N23			x	x		x			
N24			x	x		x			
N25			x	x		x			
N26						x			
N27						x			
N28						x			

α Schedules	ϕ Schedule	Technique	Nominal Model Attitude		
			α , deg	β , deg	ϕ , deg
A	0	Pitch-Pause	-4, -2, 1 0, 1, 2, 4, 6, 8, 10, 12, 14,	0	0
B	0	Sweep	-6→14	0	0
B	90		0	-6→14	90
B	-90		0	14→-6	-90
B	180		6→14	0	180
C	0		14→6	0	0
C	180		-14→6	0	180
0	D		0	0	-170→170

Notes: 1. Model Attitude Schedules

2. All data were taken at a nominal Reynolds number of 0.18 million based on model base diameter except for the N22*M5*A17 configuration, where data were also acquired at 3.6 million per ft at Mach 2.0, 1.1, and 1.3, and 3.6 million per ft at Mach 3.0.

* These data are presented in this report.

NOMENCLATURE

C_A	Forebody axial-force coefficient, $C_{A_t} - C_{A_b}$
C_{A_b}	Base axial-force coefficient, $-(p_b - p_\infty)/q_\infty$
C_{A_0}	Forebody axial-force coefficient at $\alpha = 0$
C_{A_t}	Total axial-force coefficient, total axial force/ $q_\infty S$
C_m	Pitching-moment coefficient, pitching moment/ $q_\infty S d$ (see Fig. 4 for moment reference)
C_{m_α}	Slope of pitching-moment coefficient versus α curve at $\alpha = 0$, 1/deg
C_N	Normal-force coefficient, normal force/ $q_\infty S$
C_{N_α}	Slope of normal-force coefficient versus α curve at $\alpha = 0$, 1/deg
d	Model base diameter, 1.200 in.
M_∞	Free-stream Mach number
PB1-PB4	Model base pressure probes 1-4, respectively
PBD	Model base pressure measured with fast response transducer
P_0	Tunnel stilling chamber pressure, psia
p_b	Base pressure, psia
p_∞	Free-stream static pressure, psia
q_∞	Free-stream dynamic pressure, psia
Re_d	Reynolds number based on free-stream conditions and model base diameter
R_N/R_B	Model spherical nose radius ratioed to model base diameter, nose bluntness
S	Model base area, 1.131 in. ²
T_0	Tunnel stilling chamber temperature, °R
$X, Y,$	Model nose coordinates along and perpendicular to the nose centerline, respectively, in.

XCP	Model center-of-pressure location measured in calibers aft of the nose-midbody juncture, $-C_m/C_N$
α	Angle of attack, deg
β	Model side-slip angle, deg
ϕ	Model roll angle, deg

CONFIGURATION DESIGNATION

The model configuration is designated by a sequence of groups of letters and numbers separated by asterisks. The various groups indicate specific configuration components as indicated below. See Fig. 4 for details of the model and components.

NXX	Model nose section
MXX	Model midbody section
A17	Model afterbody section